ASCE

Resolved CFD-DEM Modeling of Suffusion in Gap-Graded Shaped Granular Soils

Ya-Jing Liu[1]; Zhen-Yu Yin[2]; Shuai Huang, Ph.D.[3]; Zhengshou Lai[4]; and Chuang Zhou[5]

Abstract: The effect of particle shape on the suffusion of gap-graded soils is an essential although poorly understood subject in geotechnical engineering that requires further investigation. This work presents a macroscale and microscale numerical investigation into the effect of particle shape on the suffusion of gap-graded granular materials. Rounded, elliptical, and convex particles with the same volume-equivalent diameter and varying shape coefficients were generated and used to produce samples. Next, a series of resolved coupled computational fluid dynamics (CFD) and discrete-element method (DEM) simulations were performed to provide evidence of the effect of particle shape on the suffusion susceptibility of gap-graded soils. The evolution of particle orientation, moment, and drag force coefficient were analyzed to determine the mechanisms by which particle shape exerts influence. The fine angular particles under seepage flow were found to adjust their orientation, reducing the projected area of the particle perpendicular to the fluid flow direction. Fine particles in high-flow-velocity regions had a smaller projected area and drag force coefficient. The continuous rotation of the irregularly shaped particles during suffusion implies that their migration should counteract the moments exerted by the surrounding particles. In the sample containing various irregularly shaped particles, the initial position of the most irregularly shaped particle was closer to the outlet, implying that irregularly shaped particles are less susceptible to suffusion. **DOI: 10.1061/JGGEFK.GTENG-11891.**

Author keywords: Granular material; Internal erosion; Computational fluid dynamics (CFD); Discrete-element method (DEM); Particle shape; Micromechanics.

Introduction

Suffusion, which is a major type of internal erosion affecting gap-graded soils, involves the selective loss of the fine fraction within a coarse soil matrix under the action of seepage. The geometrical criteria of suffusion proposed in the literature usually are based on the profile of the particle-size distribution (PSD) curve or the equivalent diameter of voids between soil particles (Kenney and Lau 1985; Burenkova 1993; Indraratna et al. 2011). However, natural soil and sand particles usually are irregularly shaped, meaning that the particle length varies along different axes. Therefore, basing the geometrical criteria on a single particle-size parameter is likely to lead to a failure to evaluate suffusion susceptibility properly in some cases. Several studies that explored the effects of particle shape (e.g., aspect ratio and angularity) on suffusion in laboratory experiments (Marot et al. 2012; Fleshman and Rice 2014; Slangen and Fannin 2017; Maroof et al. 2021) reported that an increase in particle aspect ratio and angularity caused a reduction in hydraulic conductivity and an increase in the suffusion resistance. Numerical analysis (Guises et al. 2009) revealed that the coordination number of a granular packing increased with the increase of aspect ratio of the constituent particles until it reached a plateau for the largest aspect ratios (>1.8). A larger coordination number contributes to the retention of the fine particles, and accordingly increases the soil's erosion resistance (Shire et al. 2014; Liu et al. 2020b). One study based on the capillary tube model (Dallo and Wang 2016) found that irregularly shaped particles decreased the mean diameter of pores and increased the probability of fine-particle clogging.

In recent years, numerical experiments exploring such problems have been carried out mainly using coupled computational fluid dynamics (CFD) and the discrete-element method (DEM), including some recent works on polyhedral particles (Xiong et al. 2021; Zhou et al. 2023). The unresolved CFD-DEM method is frequently employed in these studies, where the particle diameter is smaller than one-third of the CFD cell length (Link et al. 2005), and the local volume-averaged Navier-Stokes equation is solved. Interaction force (e.g., drag force) between fluid and particle is calculated by empirical equations deduced from laboratory experiments, such as a single particle settling in the liquid (Di Felice 1994). For irregularly shaped particles, empirical drag force models are inadequate for accurately representing the fluid-induced drag force and moment (Shen et al. 2022). Due to the limitations of the method, the influence of some key factors (e.g., particle orientation, aspect ratio, and acting moment) on suffusion remains elusive. Previous research suggests that these factors significantly affect particle movement and the characteristics of the fluid field (Ma et al. 2017; Liu et al. 2020a).

The resolved CFD-DEM method based on immersed boundary method (IBM) has the capacity to directly resolve drag forces exerted on particles, thereby eliminating the need for empirical drag force models. When the CFD mesh size is sufficiently refined, the

[1]Lecturer, College of Civil Engineering, Zhejiang Univ. of Technology, China; Associate Researcher, Center for Balance Architecture, Zhejiang Univ., Hangzhou 310000, China. Email: yajing_liu@zju.edu.cn

[2]Professor, Dept. of Civil and Environmental Engineering, Hong Kong Polytechnic Univ., Hung Hom, Kowloon, Hong Kong 999077, China (corresponding author). Email: zhenyu.yin@polyu.edu.hk

[3]Dept. of Civil and Environmental Engineering, Hong Kong Polytechnic Univ., Hung Hom, Kowloon, Hong Kong 999077, China. Email: shuai.huang@polyu.edu.hk

[4]Associate Professor, School of Civil Engineering, Sun Yat-Sen Univ., Zhuhai 519082, China. Email: laizhengsh@mail.sysu.edu.cn

[5]Ph.D. Candidate, Dept. of Civil and Environmental Engineering, Hong Kong Polytechnic Univ., Hung Hom, Kowloon, Hong Kong 999077, China. Email: chuang.zhou@polyu.edu.hk

Note. This manuscript was submitted on April 29, 2023; approved on October 26, 2023; published online on January 25, 2024. Discussion period open until June 25, 2024; separate discussions must be submitted for individual papers. This paper is part of the ***Journal of Geotechnical and Geoenvironmental Engineering***, © ASCE, ISSN 1090-0241.

IBM method exhibits greater precision and reasonability in capturing fluid–particle interaction forces. This method is also applicable in the context of the lattice Boltzmann method–discrete-element method (LBM-DEM) coupling approach (Feng and Michaelides 2004; Kang and Hassan 2011).

In view of the aforementioned issues, this study investigate the effects of the particle aspect ratio and angularity on the suffusion susceptibility of gap-graded solids based on resolved CFD-DEM simulations. A systematic numerical simulation of suffusion was performed on samples with nine different particle shapes. The simulated macroresponse of the eroded particle mass was interpreted from the micromechanical perspective, including the evolution of particle orientation, drag force, and coordination number.

Resolved CFD-DEM Method and Irregularly Shaped Particle Generation

The resolved CFD-DEM used in this study consisted of three main ingredients: CFD, DEM, and the immersed boundary method (Peskin 1972; Hager et al. 2014; Shen et al. 2022). CFD and DEM were employed to model fluids and dispersed particles with interparticle interactions, respectively. Fluid–particle interaction was fully resolved via the immersed boundary method (Peskin 1972). Specifically, the fluid domain and particle domain were assumed to overlay each other, with the fluid mesh size much smaller (e.g., about 1/8–1/10) than the particle size (Hager et al. 2014). The effect of particle motion on the fluids was accounted for by enforcing the fluid velocity to be the same as that of the particles, whereas the force exerted on the particles by the fluids was computed by integrating the pressure gradient and viscous stress over the surface of the particles. The drag force acting on irregularly shaped particles during suffusion was calculated directly using the resolved CFD-DEM method, thus eliminating the reliance on empirical drag force models. Furthermore, the method employed in this study enables the capture of particle rotation and moments during suffusion, which in turn facilitates the investigation of their impacts on the suffusion process. The suffusion behavior of mixed-shape particles was examined and compared with that of single-shape particles. Therefore, fluid–particle interaction was fully resolved, and the particle size and shape effect could be considered explicitly. For the sake of completeness, the formulation of the DEM, CFD, and CFD-DEM coupler is described briefly in the following section; Hager et al. (2014) and Shen et al. (2022) presented more details.

Governing Equations for DEM

DEM is a widely used approach for simulating the behavior of dispersed particles based on Newton's second law of motion (Cundall and Strack 1979). At any time t, the equations governing the translational and rotational motion of particle i are written as follows:

$$m_i \frac{d\mathbf{U}_i}{dt} = \sum_{j=1}^{n_i^c} \mathbf{F}_{ij}^c + \mathbf{F}_i^f$$

$$\mathbf{I}_i \frac{d\boldsymbol{\omega}_i}{dt} + \boldsymbol{\omega}_i \times (\mathbf{I}_i \cdot \boldsymbol{\omega}_i) = \sum_{j=1}^{n_i^c} \mathbf{M}_{ij}^c + \mathbf{M}_i^f \tag{1}$$

where m_i and $\mathbf{I}_i$ = mass and moment of inertia tensor of particle i, respectively; $\mathbf{U}_i$ and $\boldsymbol{\omega}_i$ = transitional and angular velocities of particle i, respectively; and n_i^c = number of total contacts for particle i. The forces involved include the contact force and torque acting on particle i by particle j (i.e., $\mathbf{F}_{ij}^c$ and $\mathbf{M}_{ij}^c$), as well as the particle–fluid interaction force and torque acting on particle i (i.e., $\mathbf{F}_i^f$ and $\mathbf{M}_i^f$). Gravitational force was not considered in this study. This work used the linear Hooke's contact law in conjunction with Coulomb's friction law to evaluate interparticle contact forces.

The modeling of nonspherical particles employs polyhedral particles, wherein the significance of the shape edge, a vital geometrical feature, is emphasized (Zhao et al. 2015). This study adopted the Hertz–Mindlin contact model, which calculates the normal and tangential forces based on the overlap between two interacting particles. In the case of polyhedral particles, this overlap corresponds to the intersection of two sets of inequalities. The determination of contact between two polyhedral particles is ascertained by establishing a common plane (Cundall 1988). If a plane can distinctly separate all vertices of Particle A on one side from all vertices of Particle B on the other, it signifies the absence of contact between the two particles. Conversely, when such a differentiating plane cannot be established, it indicates that the particles are in contact.

The normal orientation of contact for spheres is defined as the vector connecting two spherical centers, whereas for polyhedral particles, the vector is determined utilizing the least-squares fitting method (Elias 2014). Based on the contact line, which can be obtained by solving the set of bounding faces inequalities, a fitting plane can be determined. The vector perpendicular to the fitting plane through the mass center of overlap is defined as the normal contact direction of polyhedral particles. A comprehensive introduction to the contact detection and overlap calculation of polyhedral particles has been well documented in the work of Zhao et al. (2015).

Governing Equations for CFD

For simplicity, this work focused on a single-phase incompressible fluid. The CFD method solves the following continuity equation and Navier–Stokes equation:

$$\frac{\partial \rho_f}{\partial t} + \nabla \cdot (\rho_f \mathbf{U}_f) = 0$$

$$\frac{\partial (\rho_f \mathbf{U}_f)}{\partial t} + \nabla \cdot (\rho_f \mathbf{U}_f \otimes \mathbf{U}_f) = -\nabla p + \nabla \cdot (\mu_f \nabla \otimes \mathbf{U}_f) + \rho_f g \tag{2}$$

where $\mathbf{U}_f$ = average velocity of a fluid cell; p = fluid pressure; ρ_f and μ_f = fluid density and viscosity, respectively; $\mathbf{g}$ = gravitational acceleration; and $\otimes$ denotes the direct product of two vectors. The influence of particle motion on the fluid field is implemented by enforced equality between particle velocity ($\mathbf{u}_s$) and fluid cell velocity ($\mathbf{U}_f$), as follows:

$$\mathbf{u}_s = \mathbf{U}_i + \boldsymbol{\omega}_i \times \mathbf{r}_i \quad \text{in } \Omega_p$$

$$\mathbf{U}_f = \widehat{\mathbf{U}_f} \alpha_f + \mathbf{u}_s (1 - \alpha_f) \quad \text{in } \Omega \tag{3}$$

where $\widehat{\mathbf{U}_f}$ = fluid velocity before correction; $\mathbf{r}_i$ = positive vector relative to the particle centroid; α_f (i.e., void fraction) = proportion of fluid in a cell calculated by a multisphere mapping algorithm (Hager et al. 2014), and $\alpha_f = 0$ when the fluid cell is entirely occupied by a particle; and Ω and Ω_p are the whole simulation domain and particle domain, respectively.

Hydraulic Force on Particles

The hydraulic force exerted on the particles by fluids is calculated by integrating the fluid stress over the particle surface as follows:

J. Geotech. Geoenviron. Eng., 2024, 150(4): 04024008

$$t = \sigma \cdot n \ on \ \partial\Omega_p$$
$$\sigma = -pI + \tau = -pI + \mu_f(\nabla \otimes \mathbf{U}_f + \mathbf{U}_f \otimes \nabla) \quad (4)$$

where $\boldsymbol{\sigma}$ = fluid stress for a Newtonian fluid; $\mathbf{n}$ = outward normal vector of particle surface; $\mathbf{I}$ = unity tensor; and Ω_p and $\partial\Omega_p$ = particle domain and particle surface, respectively. With recourse to the divergence theorem and transferring all of the hydraulic forces to particle centroids, the hydraulic force subjected by the particles can be calculated as

$$\mathbf{F}_{i,f} = \oint_{\partial\Omega_p} \mathbf{t} dS = \oint_{\partial\Omega_p} \boldsymbol{\sigma} \cdot \mathbf{n} dS = \int_{\Omega_p} \nabla \cdot \sigma dV = \int_{\Omega_p} (-\nabla p + \nabla \cdot \tau) dV$$
$$\mathbf{M}_{i,f} = \oint_{\partial\Omega_p} \mathbf{r} \times \mathbf{t} dS = \oint_{\partial\Omega_p} \mathbf{r} \times (\boldsymbol{\sigma} \cdot \mathbf{n}) dS = \int_{\Omega_p} \mathbf{r} \times \nabla \cdot \sigma dV$$
$$= \int_{\Omega_p} \mathbf{r} \times (-\nabla p + \nabla \cdot \tau) dV \quad (5)$$

In addition, in a discretized form, the force and moment are calculated as

$$\mathbf{F}_{i,f} = \sum (-\nabla p + \nabla \cdot \boldsymbol{\tau}) V_c (1 - \alpha_f) = \sum \mathbf{f}_{IB} V_c (1 - \alpha_f)$$
$$\mathbf{M}_{i,f} = \sum \mathbf{r} \times (-\nabla p + \nabla \cdot \boldsymbol{\tau}) V_c (1 - \alpha_f)$$
$$= \sum \mathbf{r} \times \mathbf{f}_{IB} V_c (1 - \alpha_f) \quad (6)$$

where V_c = volume of a fluid cell; $\boldsymbol{\tau} = \mu_f(\nabla \mathbf{U}_f + (\nabla \mathbf{U}_f)^T)$; and $\mathbf{f}_{IB} = -\nabla p + \nabla \cdot \boldsymbol{\tau}$ = fluid force for a Newtonian fluid.

The approach employed for fluid dynamics computation in this study involved utilizing the finite-volume method (FVM) to solve the Navier–Stokes equation. Other common method for fluid dynamics computation includes the lattice Boltzmann method, smoothed particle hydrodynamics (SPH), and arbitrary Lagrange–Euler (ALE) method. The finite-volume method was adopted in this study due to the computational efficiency. For instance, smoothed particle hydrodynamics constitutes a discrete Hamiltonian system comprised of material points of constant mass that evolves over time, and thus SPH requires a neighbor-searching procedure for every particle at each time step, which significantly impacts code efficiency (Douillet-Grellier et al. 2019). In contrast, both the lattice Boltzmann method and the FVM exhibit comparable computational efficiency, especially when dealing with simpler fluid models; LBM is superior in dealing with complicated boundaries, but it requires specific algorithms and meticulous consideration. Because this study involved a cubic fluid domain with an inlet and outlet, boundary conditions which are relatively simple and straightforward for the LBM and FVM, the FVM was suitable, and was favored because the authors possess substantial experience with FVM-based open-source code (Liu et al. 2020b, 2021, 2023; Qian et al. 2021; Zhou et al. 2023). The computational efficiency of the ALE method is higher than that of the FVM (Xiao et al. 2017), and the ALE-DEM coupling approach remains unreported (Wang et al. 2022).

Irregularly Shaped Particle Generation and Shape Quantification

A simple method based on spherical harmonics (SH) was adopted to generate virtual particle shapes with prescribed shape features (Wei et al. 2018). SH is a complete set of orthogonal functions defined on the surface of a sphere. The coordination of the vertices on a particle surface can be represented by SH expansion as follows (Press et al. 1992):

$$\begin{pmatrix} x(\theta,\phi) \\ y(\theta,\phi) \\ z(\theta,\phi) \end{pmatrix} = \begin{pmatrix} \sum_{l=0}^{l_{\max}} \sum_{m=-l}^{l} c_{x,l}^m Y_l^m(\theta,\phi) \\ \sum_{l=0}^{l_{\max}} \sum_{m=-l}^{l} c_{y,l}^m Y_l^m(\theta,\phi) \\ \sum_{l=0}^{l_{\max}} \sum_{m=-l}^{l} c_{z,l}^m Y_l^m(\theta,\phi) \end{pmatrix} \quad (7)$$

where Y_l^m and $c_{x,l}^m$, $c_{y,l}^m$, and $c_{z,l}^m$ = spherical harmonic functions and coefficients of degree l and order m, respectively; and $l_{\max}$ = maximum SH degree used to reconstruct a particle surface.

The particle aspect ratio (AR) is characterized by the mean value of the elongation index (EI $= p_2/p_1$) and flatness index (FI $= p_3/p_2$)

$$\text{AR} = \frac{\text{EI} + \text{FI}}{2} \quad (8)$$

where p_1, p_2, and $p_3 (p_1 \geq p_2 \geq p_3)$ are the three principal dimensions of a particle, and are determined by principal component analysis (Zhou and Wang 2017). Numerous techniques exist for characterizing particle aspect ratio (Ersoy and Waller 1995; Hentschel and Page 2003; Blott and Pye 2008; Suh et al. 2017; Lai and Chen 2019). The approach chosen for this study is a straightforward concept and involves simple calculations, but results in closely related elongation and angularity values for particles with different shapes. As Suh et al. (2017) indicated, the aspect ratio of natural sand, computed as $d_{\max}/d_{\min}$, typically falls within the range 1–5. Applying the shape parameter algorithms utilized by Suh et al. (2017), the particles in this study had aspect ratios of 1, 4, and 16. These values can effectively represent both standard and extremely irregular particle shapes.

The particle angularity (AG) is controlled by a rotation-invariant SH factor d_{2-8}/d_1

$$\frac{d_{2-8}}{d_1} = \sum_{l=2}^{8} \frac{d_l}{d_1}$$
$$d_l = \sqrt{\sum_{i\in(x,y,z)} \sum_{m=-l}^{l} \|c_{i,l}^m\|^2} = \sqrt{\sum_{i\in(x,y,z)} \sum_{m=-l}^{l} c_{i,l}^m c_{i,l}^{m*}} \quad (9)$$

where * denotes the conjugate transpose. The SH coefficients, $c_{x,l}^m$, $c_{y,l}^m$, $c_{z,l}^m$, are constructed in two steps. First, a first-degree ellipsoid (FDE) with specified aspect ratios is generated and used to calculate d_1. Second, the coefficient matrices of SH degrees between 2 and 8 (i.e., $d_2 - d_8$) are constructed from the value of d_{2-8}/d_1. Zhao et al. (2017), Wei et al. (2018), and Lai and Chen (2019) provided more details about the irregularly shaped particle generation method. Fig. 1 shows the nine randomly generated particles with three different aspect ratios (i.e., AR = 1.0, 1.9, and 4.2) and angularities (i.e., $d_{2-8}/d_1 = 0$, 0.4, and 0.8), which were used in a series of

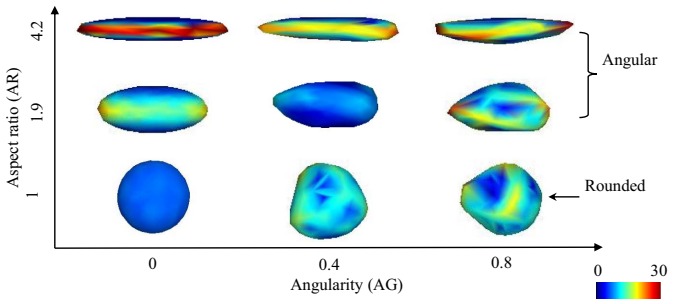

Fig. 1. Nine randomly generated particles with different shape coefficients (The legend indicates mean value of surface curvature).

suffusion simulations. In subsequent sections, rounded particles refers to the particles with AR = 1.0, whereas angular particles refers to those with AR = 1.9 and 4.2. The selection of AR and AG values served to clearly distinguish particle shapes across three distinct levels. These nonstandard integer values were derived from integer parameters (e.g., 1, 2) within the particle generation method.

Validation of the Method

Single Particle Settling in Water

To validate the CFD-DEM methodology, a laboratory experiment conducted by Guo et al. (2018) on the free settling of ellipsoidal particles was used for comparison with the results of numerical simulation. Fig. 2(a) shows the experiment setup, which involved releasing a nonspherical particle, generated by a three-dimensional (3D) printer, into a cylinder filled with water, in which it sank freely under the force of gravity. As the velocity increases, the drag force exerted on the particle gradually increases until it equilibrates with gravity, resulting in a constant velocity known as the free settling velocity. The volume equivalent sphere diameters (dpe) of the ellipsoidal particles used in the experiment are 7.6 and 9.8 mm, respectively, and a density of 1,031 kg/m^3 at room temperature. Detailed test conditions and particle properties were presented by Guo et al. (2018). The CFD-DEM simulation used a similar-sized particle as in the physical experiment, with an aspect ratio of 1.3. The dimensions of the CFD domain were 40 × 40 × 110 mm, which was large enough to ensure negligible border effects. Fig. 2(b) shows a schematic representation of the simulation setup. Table 1 summarizes the key parameters for the validation model.

Fig. 3 shows the validation case results, including the predicted and experimental velocities of particles in water. The coupled CFD-DEM method accurately predicted the particle velocity, with a maximum percentage difference of less than 5% compared with experimental data. This outcome highlights the predictive capability of the CFD-DEM method in capturing particle–fluid interaction forces for a single particle. The disparity between the simulation and experimental data probably resulted from the irregular shape of the particle, which complicates the accurate identification of solid–liquid interfaces. Additionally, there appears to have been an imprecision in calculating the pressure and velocity field around the irregularly shaped particle. The numerical solution for the Navier–Stokes equation necessitates the transformation of a volume integral into a surface integral using the divergence theorem. Consequently, it is crucial to carefully address and enhance the accuracy of the calculated velocity at the surface of the cell, particularly for cells situated at the fluid–particle interface.

Particle Cluster Settling in Water

Pal and Kulkarni (2023) conducted experiments focusing on particle clusters settling within a tranquil liquid environment in a container.

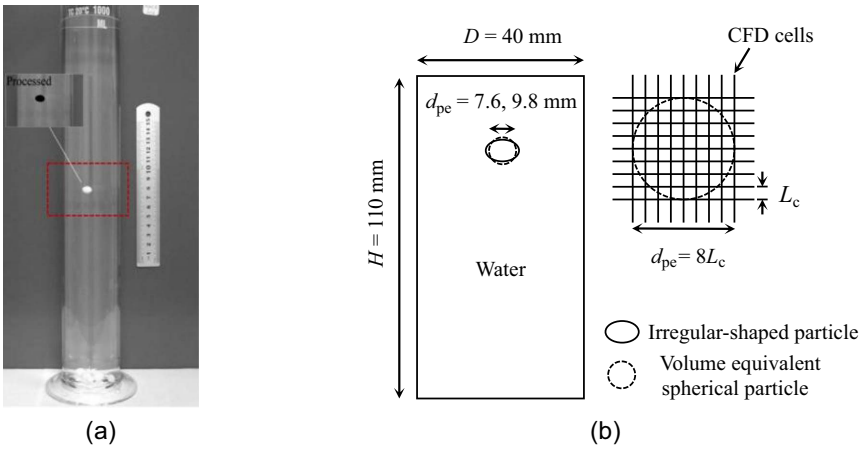

Fig. 2. Diagram of free settling experiments: (a) experiment (reprinted from *Particuology*, Vol. 39, Y. Guo, Y. Yang, X. Yu, "Influence of particle shape on the erodibility of non-cohesive soil: Insights from coupled CFD–DEM simulations," pp. 12–24, © 2018, with permission from Elsevier); and (b) CFD-DEM model.

Table 1. Summary of model parameters and settings for validation model

Content	Model parameter	Single-particle settling	Particle cluster settling
Physical model	Sample dimensions, $L \times W \times H$ (mm)	40 × 40 × 110	150 × 150 × 100
	Simulation time (s)	1.5	0.5
CFD	Cells	60 × 60 × 165	360 × 360 × 245
	Fluid viscosity, μ_f (Pa · s)	1×10^{-3}	
	Density, ρ_f (kg/m^3)	1,000	
	Timestep (s)	1×10^{-3}	
DEM	Particle density, ρ_p (kg/m^3)	1,031	1,580
	Elastic modulus, E (MPa)	1×10^8	
	Poisson's ratio, υ	0.3	
	Friction coefficient, μ_p	0.5	
	Timestep (s)	1×10^{-6}	

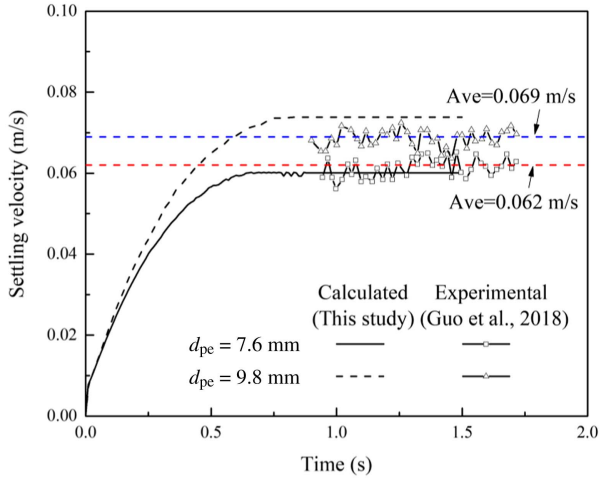

Fig. 3. Evolution of free settling velocities for irregularly shaped particles in the physical experiments and the simulations.

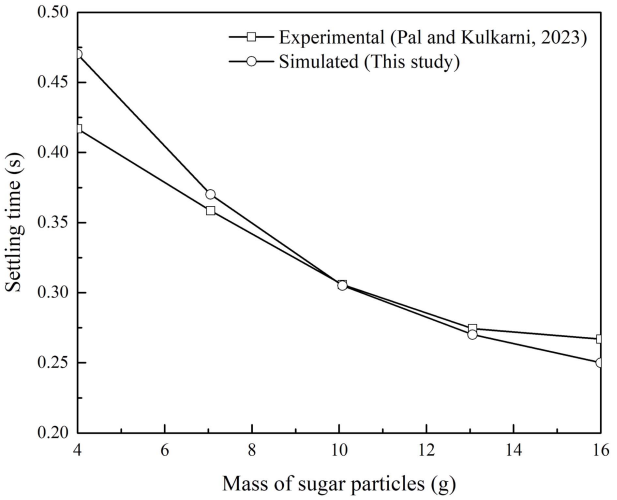

Fig. 5. Settling time versus mass of sugar particles in experiments and simulations.

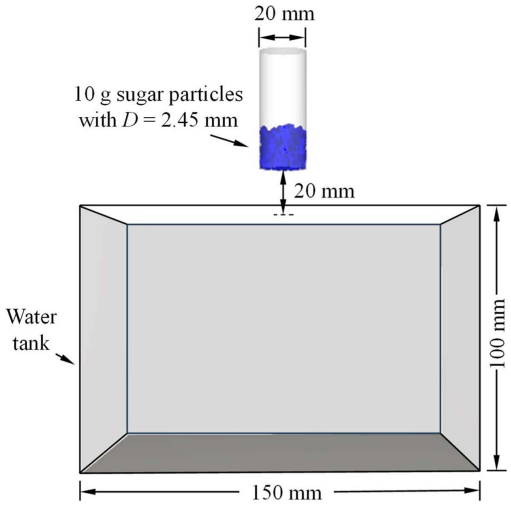

Fig. 4. Model setup for settling of particle cluster.

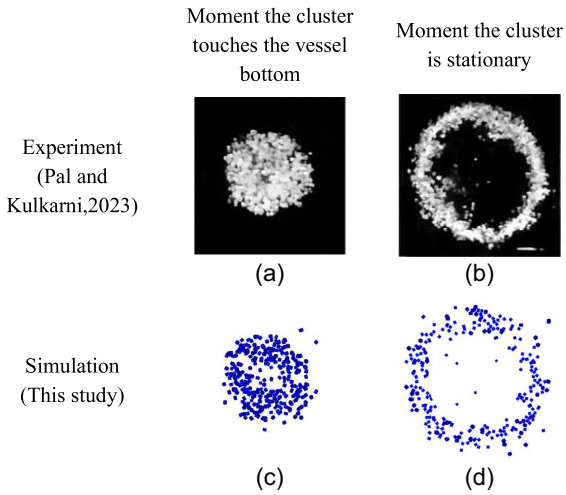

Fig. 6. Sequence of cluster spreading after collision with the vessel bottom surface.

Their findings revealed a significant correlation between the settling time, the spreading time of the sugar cluster, and its initial mass. Furthermore, the dynamic changes in the cluster's morphology during the settling process were well documented. Fig. 4 shows the validation model setup consistent with the experiment. The sugar particle model was designed with a cubic shape, measuring 2.45 mm on each side, similar to the dimensions in the experiment. A particle-to-fluid cell size ratio of 6 was adopted for expedited calculation. Table 1 lists the properties of the particle and fluid adopted in the simulation.

Fig. 5 shows the impact of the total initial mass of particles on settling time within a square water tank, as determined through experiments and simulations. Both sets of results indicate a decrease in settling time as the cluster mass increases, indicating that the methodology employed in this study can effectively account for the intricacies of flow fields in porous media. According to the simulation findings, particles located at the center of the cluster experience reduced fluid influence due to their enclosure by other particles, resulting in relatively lower drag forces. Consequently, particles at the cluster's center reach the tank bottom first. In the case of clusters with larger masses, the central particles are enveloped by a greater number of surrounding particles, leading to diminished drag forces and higher vertical settling velocities. Fig. 6 shows the sequence of cluster spreading after collision with the vessel bottom surface. The simulated results aligned well with the experimental findings.

The discrepancy between the experimental and simulated results arose primarily from variations in particle-size distribution and the estimation of drag forces. Notably, the particle equivalent size did not consistently measure 2.45 mm, and this value was not accurately provided in the work by Pal and Kulkarni (2023). Furthermore, the resolved CFD-DEM method should be improved to more-accurately define the interface between irregularly shaped particles and the surrounding fluids. The precise values for velocity and pressure fields around these irregularly shaped particles, as well as the drag forces, should be calculated to obtain a more reasonable result. The following section presents a detailed analysis of the performance of this method when applied to both irregularly shaped and spherical particles.

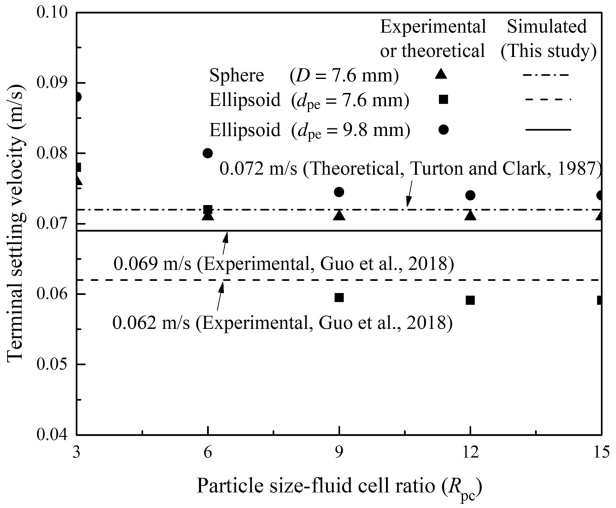

Fig. 7. Terminal settling velocity of spheres and ellipsoids under different values of R_{pc}.

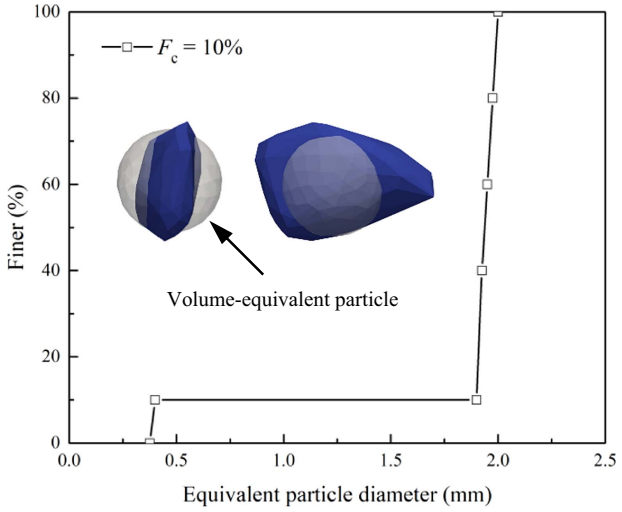

Fig. 8. Sample gradation.

Mesh Dependency Analysis

Particle sedimentation tests in Fig. 2(b) with a particle size–fluid cell ratio (R_{pc}) of 3, 6, 9, 12, 15 were performed to investigate the grid-dependent problem. Fig. 7 shows the terminal settling velocity of spheres and ellipsoids for cases with identical settings, but meshes of different grid size. For ellipsoids, the results for the two coarser meshes ($R_{pc} = 3$ and 6) differed significantly from those with the finer meshes. However, the coarser mesh representations can provide a qualitative approximation of the terminal settling velocity, i.e., larger particles typically exhibit higher terminal settling velocities. For spheres, the disparity between theoretical and simulated outcomes was relatively smaller for coarser meshes compared to ellipsoids. One likely reason for this disparity is the irregular shape of the particle, which complicates the accurate identification of solid–liquid interfaces. Additionally, there appears to be a challenge in calculating the pressure and velocity field around the irregularly shaped particle. The numerical solution for the Navier–Stokes equation necessitates the transformation of a volume integral into a surface integral using the divergence theorem. Consequently, it is crucial to carefully address and enhance the accuracy of the calculated velocity at the surface of the cell, particularly for cells situated at the fluid–particle interface.

Model Setup and Simulation Scenarios

Simulation Scenarios

A total of 17 simulation scenarios were analyzed to examine the impacts of particle aspect ratio and angularity on the suffusion behavior of gap-graded soils. For fine particles, all nine shapes in Fig. 1 were assessed individually in each scenario, and an additional scenario featured a blend of all nine fine particle shapes. The study further examined the impact of flow direction, specifically investigating cases aligned with the direction of gravity, perpendicular to the direction of gravity, and against the direction of gravity. Additionally, the study explored the influence of suffusion time. For each case, the specimen followed the PSD shown in Fig. 8. Typically, the fine contact F_c (i.e., the ratio of the mass of fine particles to that of all particles) was about 10%, yielding a representative case of particle packing with coarse particles underfilled by fine particles. A sample with a particle size ratio $D_{15c}/d_{85f} = 5.2$ (where D_{15c} and d_{85f} are the diameters of the 15% mass passing in the coarse fraction and the diameters of the 85% mass passing in the fine fraction, respectively) is internally unstable according to the Kenney and Lau criterion (Kenney and Lau 1985). The coarse particles play a crucial role in determining pore heterogeneity and flow field characteristics. For simplicity, the shape of the coarse particle remained uniform across all cases, characterized by an aspect ratio of 1.9 and an angularity of 0.8. Notably, the d_{max}/d_{min} of this particle was 4, which is a value that aligns with the shape parameter range observed in natural sand particles (Suh et al. 2017). Table 2 summarizes the settings of the 17 different simulation scenarios.

Model Geometry and Parameters

Fig. 9 shows an example of the model setup. The DEM domain consisted of a cuboid pack of nonspherical particles with an apparent packing size of about $10 \times 10 \times 10$ mm. The CFD domain was $10 \times 10 \times 12$ mm. The cross section of the CFD domain was slightly larger than the DEM sample to ensure that all fluid flowed through the sample. The CFD domain was meshed into $75 \times 75 \times 90$ cells with a mesh size of about 0.13 mm, which was about 1/3 the fine particle equivalent diameter (i.e., 0.4 mm) and 1/15 the coarse particle equivalent diameter (i.e., 2 mm).

The relatively large size of the CFD cell, which was only 3 times smaller than the fine particle, might not precisely capture the fluid dynamics around the fine particles. However, the adopted CFD cell size was 15 times smaller than the coarse particles, which adequately captured the flow field within the coarse particle matrix. The lower resolution for the fine particles was a trade-off made for computational efficiency. The mesh dependency analysis in the section "Mesh Dependency Analysis" demonstrated that the coarser mesh representations can provide a qualitative approximation of the terminal settling velocity, i.e., larger particles typically exhibit higher terminal settling velocities. In the future, specific research will be conducted to strike a balance between resolution and computational efficiency. Table 3 summarizes the model parameters and settings.

Boundary Conditions

For the CFD domain, a constant inlet velocity of 0.1 m/s was adopted for the bottom plane, the free-slip boundary condition was

J. Geotech. Geoenviron. Eng., 2024, 150(4): 04024008

Table 2. Simulation program

Simulation identity	Aspect ratio, AR	Angularity, d_{2-8}/d_1	Void ratio, e	Flow direction, θ (degrees)	Suffusion time, t (s)	Fines content, F_c (%)	No. of fine particles	No. of coarse particles
R1G1	1	0	0.65	0	15	10	2,000	144
R1G2	1	0.4	0.66	0	15			
R1G3	1	0.8	0.66	0	15, 80			
				90				
				180				
R2G1	1.9	0	0.68	0	15			
R2G2	1.9	0.4	0.69	0	15			
R2G3	1.9	0.8	0.68	0	15, 80			
R3G1	4.2	0	0.72	0	15			
R3G2	4.2	0.4	0.72	0	15			
R3G3	4.2	0.8	0.74	0	15, 80			
				90				
				180				
Mix	1–4.2	0–0.8	0.68	0	15			

Note: θ = angle between flow direction and direction of gravity (see Fig. 20, inset).

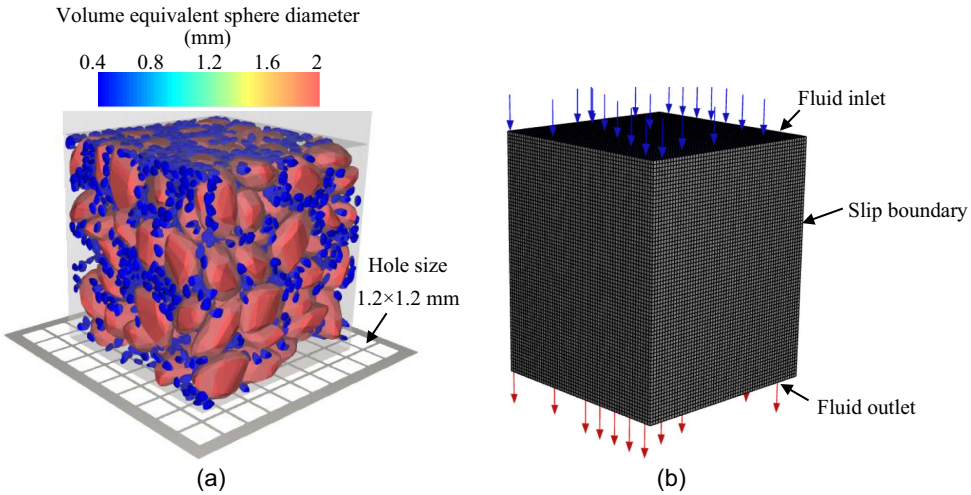

Fig. 9. Mode setup: (a) DEM sample; and (b) CFD domain.

Table 3. Summary of model parameters and settings for suffusion model

Content	Model parameter	Values
Physical model	Sample dimensions, $L \times W \times H$ (mm)	$10 \times 10 \times 12$
	Simulation time (s)	15.0
CFD	Cells	$75 \times 75 \times 90$
	Fluid viscosity, μ_f (Pa · s)	1×10^{-3}
	Density, ρ_f (kg/m^3)	1,000
	Timestep (s)	1×10^{-3}
DEM	Particle density, ρ_p (kg/m^3)	2,650
	Elastic modulus, E (N/m)	1×10^9
	Poisson's ratio, υ (N/m)	0.3
	Tangential stiffness ratio, k_t/k_n	1.0
	Friction coefficient, μ_p	0.5
	Restitution coefficient, e	0.3
	Timestep (s)	1×10^{-6}

applied to each lateral plane, and the top was taken as a free outlet with zero pressure. Given the relatively high inlet velocity, the maximum particle Reynolds number (R_p) reaches approximately 600. The following formula proposed by Eppinger et al. (2011) was used to calculate R_p:

$$R_p = \frac{\rho_f |\mathbf{U}_f| d_p}{\mu_f} \tag{10}$$

where $|\mathbf{U}_f|$ = magnitude of fluid velocity; and d_p = particle diameter. In the fluid–solid coupling problems, the particle Reynold number (R_p) commonly is used as a criterion of the flow regime, in which a low R_p value (e.g., $R_p < 1$) denotes the laminar flow, and a high R_p value (e.g., $R_p > 1{,}000$) indicates the turbulent flow (Eppinger et al. 2011). The beginning of turbulence is indicated by values of R_p in the range 1–1,000. Because the R_p was within the transition range, a laminar flow model was used for simplicity and computational efficiency in all cases.

For the boundary conditions of the DEM, a vertical pressure (i.e., $p' = 100$ kPa) was applied to the particle packing using a servocontrol algorithm on the top boundary wall. To allow particles to be eroded, a series of 1.2×1.2-mm holes (about 3 times the fine particle equivalent diameter) was set on the bottom wall. The downstream wall was fixed with zero displacement during the simulation.

Simulation Procedure

A cuboid assembly of spheres first was generated with the prescribed gradation (Fig. 8) and shape coefficient. The coarse and

fine particles were distributed uniformly in the domain surrounded by the six boundary walls. This was followed by a vertical consolidation by pressing the top wall of the sample to achieve a consolidation pressure of $p' = 100$ kPa. For this process, an interparticle contact friction value ranging from 0 to 0.5 was employed to ensure that the void ratio of each sample fell within the range 0.65–0.75. The void ratio was limited to a narrow range to minimize its influences on suffusion (Tao and Tao 2017). The relative density, D_r, of each sample was calculated using the following equation:

$$D_r = (e_{\max} - e)/(e_{\max} - e_{\min}) \tag{11}$$

where e = void ratio of the sample; and $e_{\max}$ and $e_{\min}$ = maximum and minimum void ratios of the sample, respectively. Following Salot et al.'s (2009) method, the maximum and minimum void ratios were achieved by setting the coefficients of interparticle friction to $\mu = 0.0$ and 1.0 during the isotropic compression stage of the lowest- and highest-density samples, respectively. Fig. 10 shows the relative density for each sample. In most cases, the sample's relative density was about 50%. Achieving uniform void ratios and relative densities across all samples is a challenging endeavor.

After the generation of the initial DEM sample, the seepage flow with the specified inlet velocity was imposed on the bottom of the CFD domain to model the suffusion process. The gap ratio of the sample (i.e., 5) was relatively small for irregularly shaped particles. A downward flow direction, i.e., aligned with the gravity direction, was adopted to facilitate the migration of the fine particles (Xiong et al. 2021). The initial inlet flow velocity of 0.1 m/s was applied abruptly. This higher flow velocity was chosen due to the notable rolling resistance exhibited by the irregularly shaped particles and the small gap ratio of the sample (i.e., 5). Prior research indicated that whether the flow velocity increases gradually or suddenly, it has a quantitative impact on the loss of eroded fines, rather than a qualitative impact (Liu et al. 2023). During the suffusion process, the pressure of the six surrounding walls remained constant. The fine particles underwent migration due to the seepage flow. Some became entrapped within the sample, whereas others were carried away by the flow. Previous research primarily has emphasized the latter scenario, because the fine particles exiting the sample tend to exert more-pronounced influences on the sample's mechanical behavior (Ke and Takahashi 2014; Sibille et al. 2015; Chen et al. 2016). Therefore, particular attention was directed toward particles that exited through the downstream wall; these were designated eroded particles. Particle data (including position, velocity, hydraulic force, and so forth) and all contact forces were extracted every 0.05 s during the simulations for postanalysis.

Each simulation, which modeled 15 s of physical time of suffusion, took approximately 13–15 days on an HP station with 32 Intel Xeon E52680-v4 2.4 GHz processors and 512 GB DDR4 RAM. Although the simulation duration was relatively short compared with that in a laboratory test, this duration covered the key stages of suffusion (i.e., initiation and intensified suffusion following initiation). The following sections present and interpret the simulated macroresponse of the eroded particle mass from the micromechanical perspective, including the evolution of the particle orientation, drag force, and coordination number.

Interpretation of the Simulation Results

Macro Responses of the Sample to Suffusion

Fig. 11 shows the percentage of the cumulative eroded particle mass (i.e., the mass ratio of the eroded fine particles to the initial fine particles) for different cases. Both the particle aspect ratio and angularity had an apparent influence on suffusion. The ultimate eroded particle mass decreased significantly as the aspect ratio increased when the particle angularity was the same. The angularity significantly influenced suffusion for the sample with a low aspect ratio (e.g., AR = 1), which was consistent with the observations in previous research (Qian et al. 2021). These observations imply that the aspect ratio and angularity make a significant contribution to the resistance of suffusion in gap-graded soils. Zhao et al. (2015) also demonstrated that a self-locking effect between irregularly shaped particles increases particle-to-particle occlusion, resulting in strong resistance to the fluid flow. Fig. 12 shows the correlation between the average mass of eroded particles and the shape coefficient, including the aspect ratio and angularity, which supports the aforementioned point.

Because of the low fines content adopted in this study (e.g., 10%), the influence of fine particles on the soil stress–transfer matrix was marginal. As a result, the erosion of fine particles merely triggered significant rearrangements of soil structure, which predominantly was composed of coarse particles (Shire et al. 2014). The vertical strain for each sample was within the 0%–0.4% range, indicating the stability of the soil structure in the sample (Fig. 13).

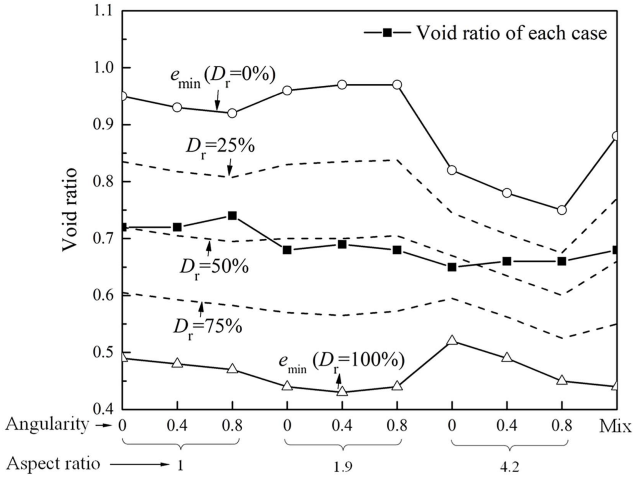

Fig. 10. Index void ratios and relative densities for different samples.

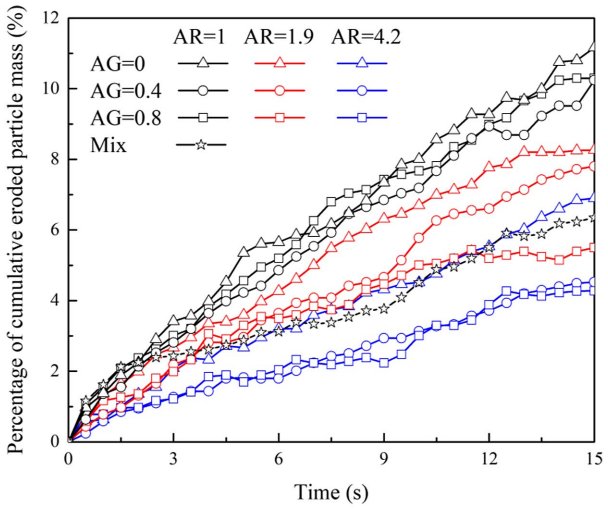

Fig. 11. Cumulative eroded mass percentage for each case.

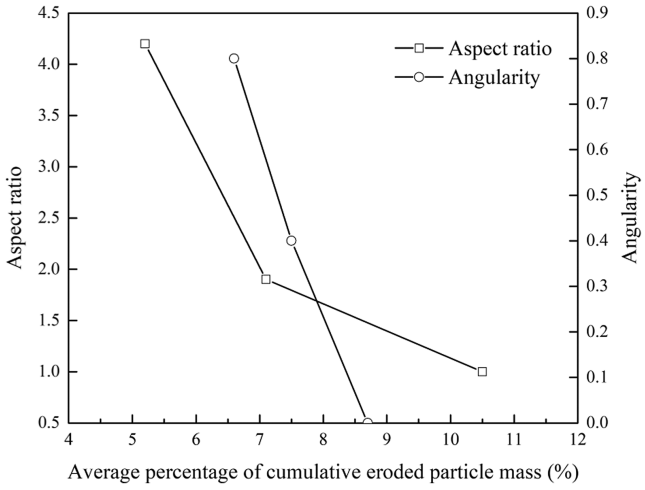

Fig. 12. Relationship between the cumulative eroded particle mass and the shape coefficients.

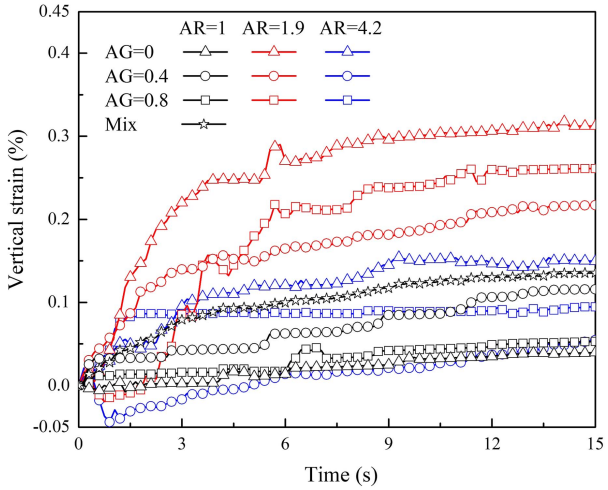

Fig. 13. Vertical strain for samples containing particles of various shapes.

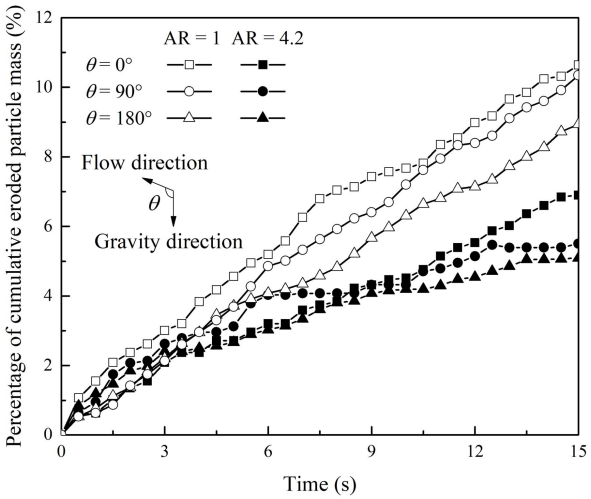

Fig. 14. Cumulative eroded mass percentage with time for AR = 1 and 4.2 under different flow directions.

Fig. 14 shows the percentage of the of the cumulative eroded particle mass for AR = 1.0 and 4.2 and AG = 0.8 under different flow directions. In each flow direction, particles with a larger aspect ratio exhibited lower eroded particle mass, indicating that particle shape consistently impacts suffusion when the flow conditions are held constant. These findings align with previous research by Qian et al. (2021) and Maroof et al. (2021), in which upward and downward flow directions were considered, respectively. In each flow direction, particles with greater irregularity experience milder suffusion effects. In addition, each sample exhibited a slightly higher eroded particle mass when the flow direction aligned with the force of gravity (Fig. 14). This observation is consistent with the findings presented by Xiong et al. (2021). However, comparing the results of this study with those of Xiong et al. (2021), it is evident that the effect of flow direction on irregularly shaped particles is considerably less pronounced than its impact on spherical particles.

The simulation time, i.e., 15 s, was relatively short compared with suffusion experiments or real-world suffusion processes. As a result, the simulation in this study mainly covered the initiation and initial developmental phases of erosion. A short simulation time was adopted for two main reasons:

1. The resolved CFD-DEM method has limited computational efficiency, rendering it unsuitable for extended calculations involving thousands of irregular particles and millions of fluid grids. In this study, a single case required an estimated computation duration ranging from 15 to 20 days when executed on a device featuring a 32-core Core i9 CPU.
2. The erosion rate (the cumulative mass of eroded soil divided by time) displayed variability across each case within a 15-s timeframe, demonstrating a discernible pattern. According to previous research, the final eroded soil mass is higher if the initial erosion rate of the sample is higher (Wautier et al. 2019; Chen and Zhang 2023; Maroof et al. 2021; Qian et al. 2021).

Although the ultimate eroded soil mass at $t = 15$ s exhibited minor variations among different samples, the erosion rates for each sample diverged. Previous research indicated that a higher initial erosion rate corresponds to a greater final eroded soil mass (Wautier et al. 2019; Chen and Zhang 2023; Maroof et al. 2021; Qian et al. 2021). This trend is illustrated in Fig. 15, which displays the eroded soil mass for AR = 1, 1.9, and 4.2 and AG = 0.8 at $t = 80$ s. Evidently, there was a substantial disparity in the eroded soil mass among these cases, aligning with the aforementioned assertion. Notably, in instances featuring a large particle aspect ratio, the eroded soil mass tended to stabilize toward a consistent value.

To reduce the variability in macroscopic results, such as deviatoric stress or volume strain, the behavior of DEM samples with different sizes is examined, and specific criteria for minimum sample size ratios or particle counts are determined (Salot et al. 2009; Kuhn and Bagi 2009; Huang et al. 2014). For example, Salot et al. (2009) observed that the influence of the number of 3D clumped-sphere particles on the macroscopic response is minimal when assemblies larger than 8,000 elements are considered. However, the standard for defining the representative volume element (RVE) in the context of suffusion has yet to be explored. This may be attributed to the nonuniform and time-dependent nature of suffusion, which poses challenges in precisely establishing the RVE. This study conducted suffusion experiments on samples that were 0.5 and 1.5 times the standard size (size ratio = 0.5 and 1.5), with ARs of 1.0 and 4.2. Larger samples, such as those twice the standard size, entail tens of thousands of particles and millions of CFD cells, resulting in significantly reduced computational efficiency.

Fig. 16 shows the cumulative eroded particle mass for AR = 1.0 and 4.2 across various sample sizes. Due to the increased computational time associated with larger samples, the analysis focused on

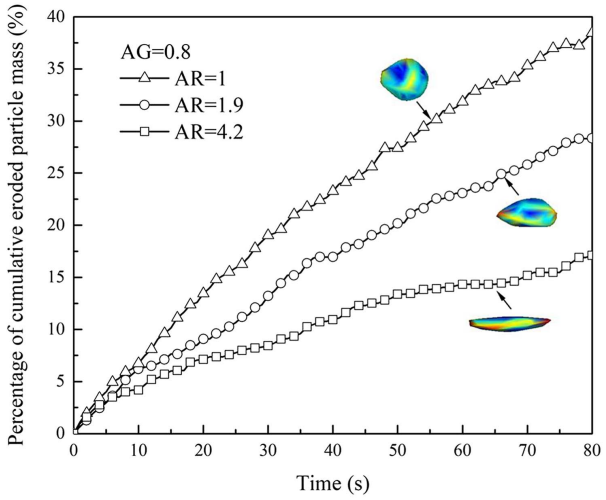

Fig. 15. Cumulative eroded particle mass for particles with varying aspect ratios at $t = 80$ s.

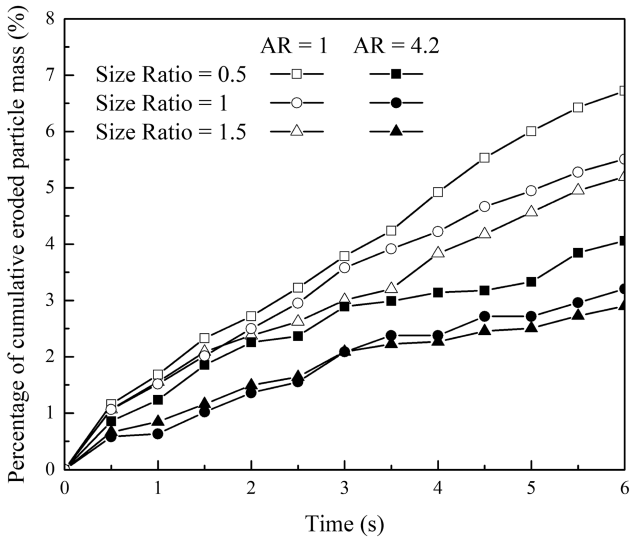

Fig. 16. Cumulative eroded particle mass in samples of different sizes.

results within a 6-s timeframe. Sample size had a quantitative influence on the results for each particle shape. Smaller samples, specifically those 0.5 times the original size, had the highest eroded particle mass. One contributing factor is the shorter distance of fine particles to the outlet, which reduced the likelihood of blockage by coarse particles. The effect of particle shape remained consistent across different sample sizes. Detailed RVE analysis for suffusion should be a focus of future research. Some studies of the spatial and temporal effects of suffusion (Moffat et al. 2011) indicated the challenges in accurately determining an RVE.

Effect of Particle Shape on Micromechanical Properties of Soil

Internal erosion occurs under the combined interplay of three factors: (1) material gradation or geometry condition, (2) critical stress condition, and (3) critical hydraulic load (Shire et al. 2014). In this study, the 10% fine content was well below the transitional fine content. It is expected that all fine particles are susceptible to suffusion because they do not contribute to the soil stress matrix. However, the geometric criterion is not invariably met. The presence of small constrictions (i.e., pore throats smaller than the fine particle), resulting from the nonuniform distribution of such features within the sample, potentially can impede the movement of fine particles (Indraratna et al. 2007; Jung et al. 2018). Pore-clogging is more likely to occur by forming bridges when many suspension particles flow simultaneously through a single constriction (Valdes and Santamarina 2006; Nguyen et al. 2019). Previous studies also have discovered that, in samples characterized by a fines content (e.g., $F_c = 10\%$ or 20%) below the transitional threshold, fine particles do not undergo complete erosion at the end of the erosion process (Bendahmane et al. 2008; Cividini et al. 2009; Liang et al. 2017). Some erosion laws adopt the residual fines content as a parameter (Cividini et al. 2009; Bonelli and Marot 2011). The following observation illustrates that fine particles with irregular shapes have a higher propensity to obstruct the voids formed by the coarse particles, consequently impeding the continued movement of upstream fine particles.

Figs. 17(a and b) show a cross section of the DEM sample and fluid velocity field for AR = 1.0 and 4.2 at $t = 0.8$ s, respectively. In both cases, many fine particles downstream were eroded due to the seepage flow. The flow velocity was lower in the region of the coarse particle, and it was greater than the inlet velocity in the voids formed by the coarse particles. For the samples with fine particles with a high aspect ratio, the transportation channel for the fluid and fine particles easily could be blocked by clusters of fine particles that consist of 3–5 elongated particles. A large aspect ratio facilitates the formation of strong contact force chains and thus further enhances the self-block effect (Yin et al. 2020). This blockage results in the retention of many irregularly shaped fine particles upstream [Fig. 17(a)].

In contrast, the fine particles with a low aspect ratio (i.e., AR = 1) exhibited a low possibility of blocking the fluid channel, resulting in the continuous migration of fine particles during suffusion. Consequently, the number of fine particles upstream was significantly lower than that in the sample with irregularly shaped particles. In addition, fluid flow in the sample with rounded particles tended to concentrate in a continuous pore channel, thereby promoting the erosion of the fine particles around the concentrated flow [Fig. 17(b)]. These observations are explained further from a microscopic view, including coordination number, drag force, and particle moment, in the following sections.

Fig. 18 shows the evolution of the coordination number of the fine particles, Z^{fine}, (i.e., the number of contacts of fine particles) during suffusion for each case; Z^{fine} is calculated as follows (Shire et al. 2014):

$$Z^{\text{fine}} = \frac{\sum_{i=1}^{N_{p,\text{fine}}} (C_i^{\text{fine-fine}} + C_i^{\text{fine-coarse}})}{N_{p,\text{fine}}} \tag{12}$$

where $N_{p,\text{fine}}$ = total number of fine particles; $C_i^{\text{fine-fine}}$ = number of contacts between fine particle i and other fine particles; and $C_i^{\text{fine-coarse}}$ = number of contacts between particle i and coarse particles.

The value of Z^{fine} was higher for the sample with a larger aspect ratio during the entire suffusion process, which is consistent with previous research (Qian et al. 2021). For the sample with a low aspect ratio (e.g., AR = 1), the number of fine–fine contacts decreased apparently at the initial stage of suffusion, which also was observed in the suffusion simulation of spherical particles (Hu et al. 2019). This was because spherical particles are prone to detach from the soil skeleton under seepage flow, leading to the collapse of the load-bearing structure constituted by the fine particles (Liu et al. 2020b). In contrast, Z^{fine} increased less during the entire suffusion

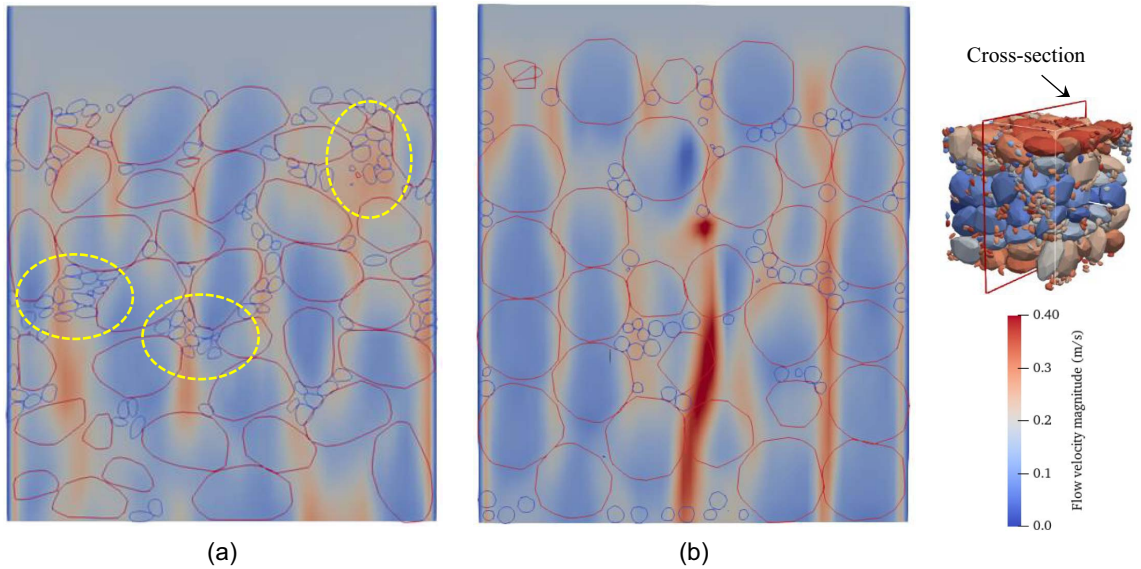

Fig. 17. Transection of DEM domains for the cases with (a) AR = 4.2, AG = 0.8; and (b) AR = 1.0, AG = 0.8 at $t = 0.2$ s.

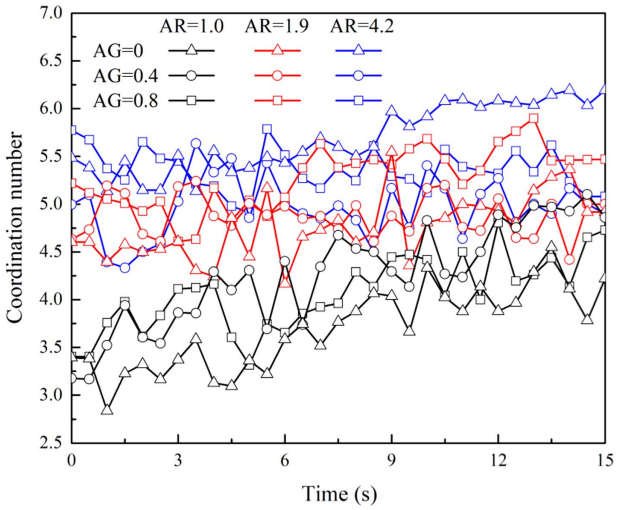

Fig. 18. Evolution of the number of fine–fine contacts during suffusion for each case.

process in the sample with a higher aspect ratio and angularity. As analyzed previously, the self-block effect enhances the stability of the load-bearing structure constituted by the angular particles under seepage flow.

Fig. 19(a) shows the distribution of particle moment for each case at the initial stage of suffusion (i.e., $t = 0.1$ s). The particles with a higher aspect ratio and angularity experienced a smaller moment. A small particle moment decreases the probability of particle rotation, increasing the stability of the fine particles under seepage flow. These results are consistent with the cumulative eroded particle mass in each case (Fig. 11). The analysis in the section "Behavior of Particle Orientation and Its Effect on Suffusion" shows that the particle orientation is responsible for the smaller moment of the angular particle. For the rounded particle (i.e., AR = 1), the particle moment was almost constant, no matter the particle's orientation.

Fig. 19(b) shows the distribution of the fluid hydraulic force exerted on the particles for each case at the initial stage of suffusion (i.e., $t = 0.1$ s). Similar to particle moment, the drag force was relatively smaller for the samples with a higher aspect ratio and

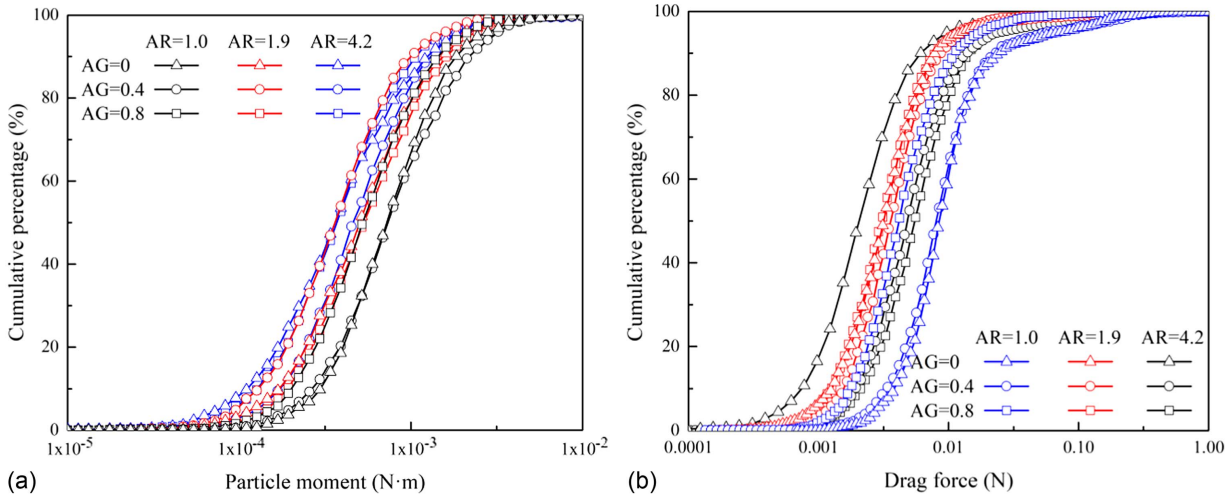

Fig. 19. For each case at the initial stage of suffusion, distribution of the (a) particle moment; and (b) drag force.

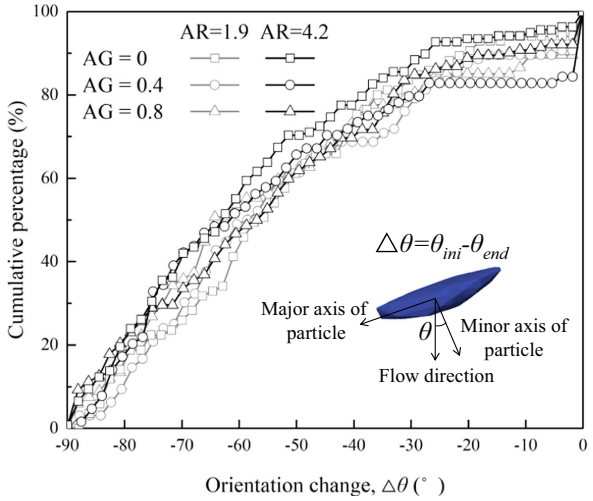

Fig. 20. Distribution of the variation of θ before and after suffusion for the cases with AR = 1.9 and 4.2.

angularity under the same inlet flow velocity. Subjecting the fine particles to a small drag force reduces the probability of particle detachment and the migration distance of the fine particles. The orientation of the angular particle determines its surrounding flow field, further influencing the drag force of the particle. When an angular particle is subjected to the action of seepage flow, it avoids detachment and migration by adjusting its orientation and the drag force applied to it. This explanation is verified in the section "Behavior of Particle Orientation and Its Effect on Suffusion" using the relationship between the particle orientation and several key influential factors of suffusion, such as flow velocity, drag force, and so forth.

Behavior of Particle Orientation and Its Effect on Suffusion

Previous research on the coupled fluid–particle problem (Ma et al. 2017; Liu et al. 2020a) has shown that particle orientation greatly influences drag force, particle motion, and flow field. This section further analyzes the evolution of particle orientation during suffusion. For the convenience of analysis, we set the longest and shortest axes of irregularly shaped particles as major and minor directions, respectively (Fig. 20, inset). The third axis was set as the medium direction. For the present simulation cases, the size of the fluid channel between the coarse particles generally was smaller than the length of the major principal axis of the fine particles (Fig. 17). Therefore, the fine particles were more likely to migrate through the channels if their long axis was relatively parallel to the course of the channel. The quantitative analysis presented in Fig. 20 shows the variation of the angle from the particle minor principal axis to the apparent flow direction of the fluid (i.e., z-direction of the model) before and after suffusion for AR = 1.9 and 4.2. The variation of the angle for each eroded particle, $\Delta\theta$, is calculated as follows:

$$\Delta\theta = \theta_{\text{ini}} - \theta_{\text{end}} \tag{13}$$

where θ_{ini} and θ_{end} = angles between particle minor principal axis and global z-axis at the initial time and the time when the particle flows out of the sample, respectively. A larger angle corresponds to a smaller particle's projected face area perpendicular to the fluid flow, as well as to less drag force on the particle. All eroded fine particles experienced an angle increase (i.e., the major principal axis of the fine particle was more parallel to the global z-axis and flow direction) during suffusion. Fig. 21 shows several snapshots of a specific fine particle during suffusion in the case of AR = 4.2 and AG = 0.8. The particle exhibited a decreased inclination angle during migration. This result is consistent with Guo et al. (2018).

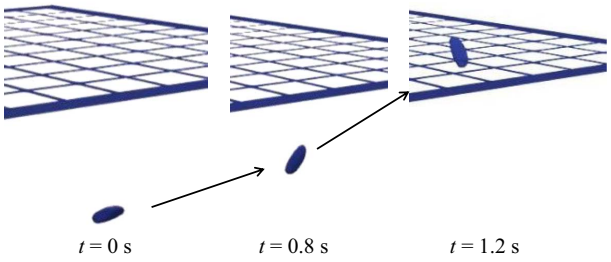

Fig. 21. Orientation evolution of a specific fine particle during suffusion in the case with AR = 4.2 and AG = 0.8.

Further insights into the evolution of particle orientation during suffusion can be gained by dividing the particle inclination angle (i.e., θ) into three groups: 0°–30°, 30°–60°, and 60°–90°. The particles corresponding to each group of inclination angle were counted. Fig. 22 shows the evolution of the particle inclination angle for the cases of AR = 4.2 during suffusion. The number of particles in the range 60°–90° increased, suggesting that the projected area of more fine particles decreased under seepage flow to avoid detachment and migration. The number of fine particles in the ranges 0°–30° and 30°–60° slightly decreased. The results indicate that elongated particles will exhibit a decreased inclination angle during their migration, resulting in decreased hydraulic forces, leading to reduced migration velocity. Therefore, an elongated particle will exhibit higher resistance to suffusion than will less-elongated particles.

We investigated the mechanism of the particle orientation change during suffusion. Fig. 23 shows the average flow velocity around the fine particles (i.e., within one diameter range from the particle centroid) at $t = 2.0$ s for the cases of AR = 1.9 and 4.2. In this example, the average fluid velocity $|\overline{\mathbf{U}_{fi}}|$ is defined as

$$|\overline{\mathbf{U}_{fi}}| = \frac{\sum_{p=1}^{n_p} |\overline{\mathbf{U}_f}(\theta_i < \theta_p < \theta_i + 10°)|}{n_p} \tag{14}$$

where $\overline{\mathbf{U}_f}$ = average flow velocity around a fine particle; $\theta_i = 0°, 10°, \ldots, 80°$; $\theta_p = \theta$ value of a fine particle; and n_p = number of fine particles that have θ_p values in the range θ_i to $\theta_i + 10°$. Because the simulations were based on resolved CFD-DEM, the flow velocity around fine particles was the true velocity of the fluid in the voids between the coarse particles. According to the results, the fine particles in the area with a higher flow velocity had a larger inclination angle (i.e., a smaller projected area perpendicular to the fluid flow direction). This implies that an angular particle subjected to seepage flow can adjust its orientation to reduce its projected face area and increase its stability (i.e., no detachment and migration). For this reason, the flow velocity causing the detachment of the angular particle was statistically higher than that of the rounded particles (i.e., AR = 1).

Fig. 24 quantitatively presents the influence of particle orientation on drag force. Specifically, the figure shows the average drag coefficient of the fine particles in different ranges of θ at $t = 2.0$ s for each case. The drag coefficient C_D is calculated as follows (Bagheri and Bonadonna 2016):

$$C_D = \frac{2\mathbf{F}_D}{-\rho_f A|\mathbf{U}_p - \mathbf{U}_f|(\mathbf{U}_p - \mathbf{U}_f)} \tag{15}$$

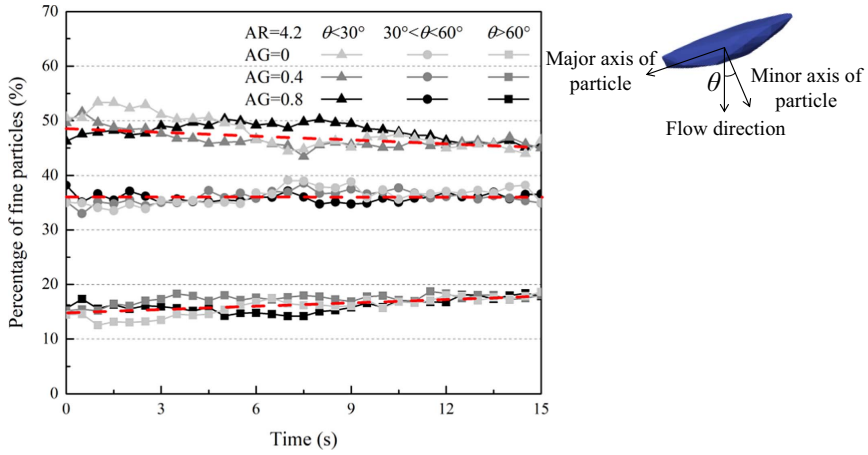

Fig. 22. Evolution of the number of the fine particles in different ranges of θ for the cases with AR = 4.2 (blue dashed line denotes the slope of the numerical results).

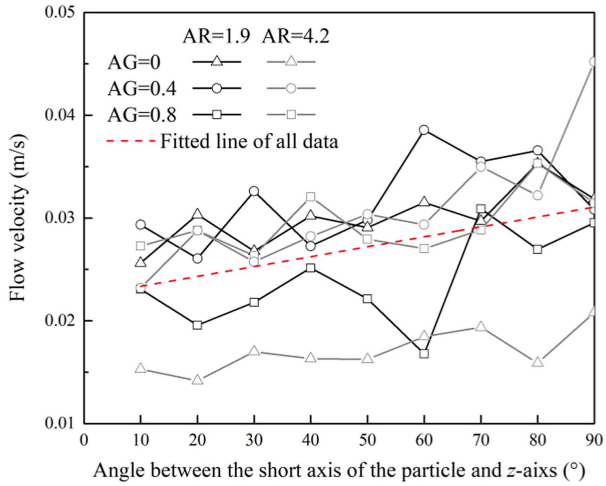

Fig. 23. Average flow velocity around the fine particles in different ranges of θ at $t = 2.0$ s for the cases with AR = 1.9 and 4.2.

where $\mathbf{F}_D$ = drag force of the particle; ρ_f = fluid density; A = reference area related to particle size (e.g., $\pi d^2/4$ for a sphere with a volume equivalent diameter of d); $\mathbf{U}_p$ = particle velocity; and $\mathbf{U}_f$ = fluid velocity around the particle (i.e.,within one diameter range from the particle centroid) in this study. The angular particles (i.e., AR = 1.9 and 4.2) with larger θ statistically had smaller drag coefficients, facilitating the stability (i.e., no detachment and migration) of these fine particles under seepage flow. The drag coefficients of the rounded particles (i.e., AR = 1) had no apparent relationship with θ, suggesting that the orientation of the rounded particle has a slight influence on drag coefficients. However, the average drag coefficient for the rounded particle was larger than that of the angular particle, consistent with the results in Fig. 19(b). The fitted lines of the results are presented in the figures to explicitly show the relationship between the two variables.

Simulation Results for Mixed Case

Natural sandy soil usually contains particles of different shapes. A suffusion case that mixed the nine kinds of irregularly shaped

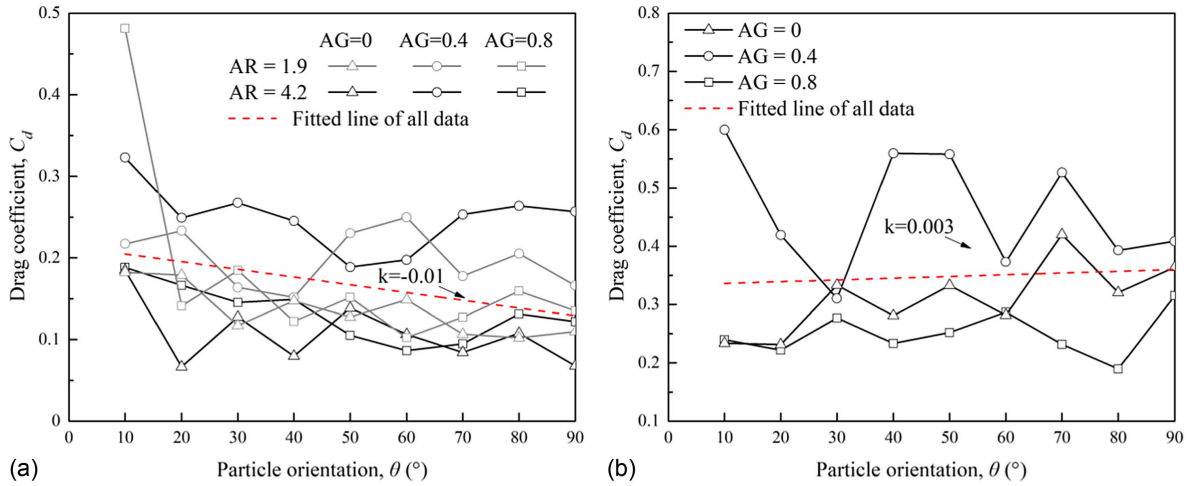

Fig. 24. Average drag coefficient of the fine particles in different ranges of θ at $t = 2.0$ s for the cases with (a) AR = 1.9 and 4.2; and (b) AR = 1.0. (k means the slope of the strait line.)

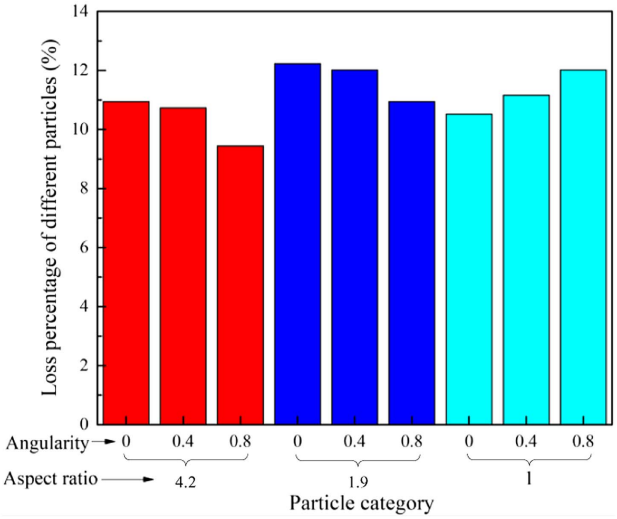

Fig. 25. Loss percentage of each kind of eroded fine particle.

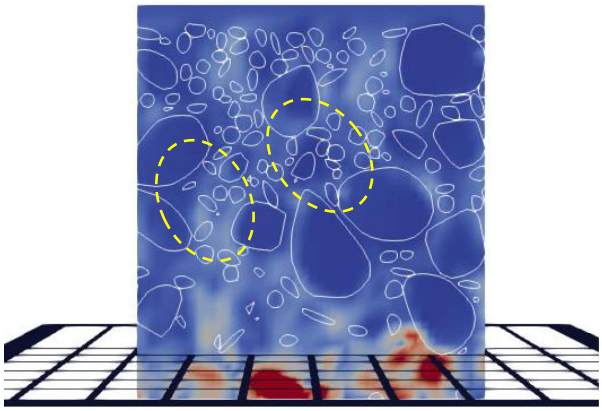

Fig. 26. Transection of the DEM and CFD domain for mixed case.

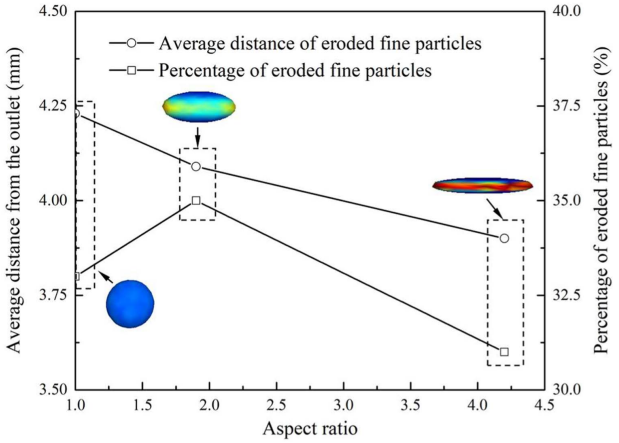

Fig. 27. Initial average distance and the percentage of eroded fine particles with different aspect ratios.

particles was performed to investigate the erodibility of different particles. Each fine particle had a diameter of 0.4 mm, and the mixed case had a fines content of 10%. Among the nine particle shapes in Fig. 8, each individual shape accounted for one-ninth of the total fine particles. The erodibility of the mixed sample was close to that of the sample with AR = 1.9 and AG = 0.4, suggesting that the addition of the irregularly shaped particles increased the suffusion resistance (Fig. 11). Fig. 25 shows the loss percentage (normalized by the total number of the eroded particles) of each kind of fine particle. Surprisingly, the loss percentages of each type of fine particle (including irregularly shaped and spherical particles) were relatively close to each other, although the susceptibility of the rounded particles to suffusion was higher than that of the irregularly shaped particles (Fig. 11). The number of eroded fine particles with a higher aspect ratio and angularity was slightly smaller.

Fig. 26 shows the cross section of the DEM sample and fluid field for the mixing case. The rounded and angular particles together blocked the flow channel upstream, preventing the continuous detachment and migration of other fine particles. The blocking cluster, which consisted of the rounded and angular particles, facilitated the retention of the rounded particles.

This study investigate the impact of particle shape on the cumulative eroded soil mass, because this mass plays a pivotal role in influencing soil mechanical behavior (Ke and Takahashi 2014; Sibille et al. 2015; Chen et al. 2017). In the context of the mixing case, the fine particles had an average irregularity level lower than that of the most irregular particle sample (e.g., AR = 4.2 and AG = 0.8) and higher than that of the sample with relatively rounded particles (e.g., AR = 1 and AG = 0). Consequently, the eroded soil mass for the mixing cases was between the values observed for these two aforementioned cases (Fig. 11). The mixed particle sample can be perceived as introducing irregular particles to the collection of rounded particles or integrating rounded particles into the assortment of irregular particles. Consequently, the former results in a reduction of the eroded soil mass, whereas the latter leads to an increase. The cumulative eroded soil mass in the mixing case aligned with the results of other cases, underscoring the impact of particle shape on suffusion.

Within the mixing case, the eroded mass of irregularly shaped particles was smaller than that of the rounded particles, yet the difference was not as significant as in the single-shape particle cases. This complexity arises from the fact that suffusion is a heterogeneous process (Israr et al. 2016), influenced by a combination of various factors. The emergence of this phenomenon can be attributed to at least two reasons:

1. Within a sample, the suffusion behavior of fine particles is influenced not only by their shape but also by their proximity to the outlet (Bendahmane et al. 2008; Liu et al. 2023). For example, an irregularly shaped particle positioned near the outlet is likely to erode sooner than a rounded particle located in the upper layer of the sample. To verify this, Fig. 27 shows the initial average distance and percentage of eroded fine particles with varying shapes. Notably, particles with a more regular shape tended to have initial positions closer to the outlet. This suggests that irregularly shaped particles located in the upper region of the sample are more difficult to erode. In addition, the fine particles with the largest aspect ratio underwent the mildest erosion (Fig. 27).
2. Suffusion is a nonuniform and time-dependent process. The limitations imposed by the number of particles and simulation time accentuate the heterogeneous nature of suffusion. Consequently, the percentage of eroded fine particles does not exhibit a monotonic decrease with changing aspect ratios (Fig. 27).

Conclusions

In this study, the immersed boundary method initially was employed to examine the suffusion behavior of irregularly shaped particles.

The drag force acting on irregularly shaped particles during suffusion was calculated directly using the resolved CFD-DEM method, thus eliminating the reliance on empirical drag force models. As a result, a detailed analysis revealed the evolution of the drag force coefficient for fine particles with different shapes during the suffusion process.

Furthermore, the method employed in this study enabled the capture of particle rotation and moments during suffusion, which in turn facilitated the investigation of their impacts on the suffusion process. For irregularly shaped particles, their detachment and migration not only must overcome the forces but also must counteract the moments exerted by the surrounding particles.

The suffusion behavior of mixed-shape particles was examined and contrasted with that of single-shape particles. The cumulative mass and initial positions of the eroded particles with varying shapes are analyzed. Based on the analyses of all simulation results, the following conclusions can be made:

1. The aspect ratio and angularity of the soil particles increased the number of contacts between fine particles, facilitating the formation of a blocking cluster and enhancing the resistance to suffusion for gap-graded sandy soils. Furthermore, the sustained rotational movement of irregularly shaped particles during suffusion increases their resistance to suffusion. This is due to the necessity of overcoming moments exerted by neighboring particles.
2. When subjected to the action of seepage flow, the long axis of an irregularly shaped particle tended to become parallel the flow direction, reducing the projected area of the particle perpendicular to the fluid flow direction. The orientation adjustment of irregularly shaped particles under seepage flow reduced the moment and drag force applied to them, increasing the suffusion resistance of the sample. Statistically, the fine particles in the local area with a higher flow velocity had a smaller projected area perpendicular to the fluid flow direction.
3. For the case containing the nine kinds of irregularly shaped particles, the addition of the irregularly shaped particle increased the suffusion resistance of the sample. The particles with a more regular shape tended to have initial positions closer to the outlet, suggesting that irregularly shaped particles located in the upper region of the sample are more difficult to erode.

Data Availability Statement

All data that support the findings of this study are available from the corresponding author upon reasonable request.

Acknowledgments

The authors gratefully acknowledge the financial supports from the Finance Science and Technology Project of Hainan Province (ZDKJ202019), the GRF project from Research Grants Council (RGC) of Hong Kong (15209119), and the National Natural Science Foundation of China (No. 52208374).

References

Bagheri, G., and C. Bonadonna. 2016. "On the drag of freely falling non-spherical particles." *Powder Technol.* 301 (Nov): 526–544. https://doi.org/10.1016/j.powtec.2016.06.015.

Bendahmane, F., D. Marot, and A. Alexis. 2008. "Experimental parametric study of suffusion and backward erosion." *J. Geotech. Geoenviron. Eng.* 134 (1): 57–67. https://doi.org/10.1061/(ASCE)1090-0241(2008)134:1(57).

Blott, S., and K. Pye. 2008. "Particle shape: A review and new methods of characterization and classification." *Sedimentology* 55 (1): 31–63. https://doi.org/10.1111/j.1365-3091.2007.00892.x.

Bonelli, S., and D. Marot. 2011. "Micromechanical modeling of internal erosion." *Eur. J. Environ. Civ. Eng.* 15 (8): 1207–1224.

Burenkova, V. V. 1993. "Assessment of suffusion in non-cohesive and graded soils." In *Proc., 1st Int. Conf. "Geo-Filters". Filters in Geotechnical Engineering*, 357–360. Rotterdam, Netherlands: A. A. Balkema.

Chen, C., and L. Zhang. 2023. "Hydro-mechanical behaviour of soil experiencing seepage erosion under cyclic hydraulic gradient." *Géotechnique* 73 (2): 115–127.

Chen, C., L. M. Zhang, and D. S. Chang. 2016. "Stress-strain behavior of granular soils subjected to internal erosion." *J. Geotech. Geoenviron. Eng.* 142 (12): 06016014. https://doi.org/10.1061/(ASCE)GT.1943-5606.0001561.

Chen, C., L. M. Zhang, and H. Zhu. 2017. "A photographic method for measuring soil deformations during internal erosion under triaxial stress conditions." *Geotech. Test. J.* 41 (1): 43–54. https://doi.org/10.1520/GTJ20170031.

Cividini, A., S. Bonomi, G. C. Vignati, and G. Gioda. 2009. "Seepage-induced erosion in granular soil and consequent settlements." *Int. J. Geomech.* 9 (4): 187–194. https://doi.org/10.1061/(ASCE)1532-3641(2009)9:4(187).

Cundall, P. A. 1988. "Formulation of a three-dimensional distinct element model-Part I. A scheme to detect and represent contacts in a system composed of many polyhedral blocks." *Int. J. Rock Mech. Min. Sci.* 25 (3): 107–116. https://doi.org/10.1016/0148-9062(88)92293-0.

Cundall, P. A., and O. D. L. Strack. 1979. "A discrete numerical model for granular assemblies." *Géotechnique* 29 (1): 47–65. https://doi.org/10.1680/geot.1979.29.1.47.

Dallo, Y. A. H., and Y. Wang. 2016. "Determination of controlling constriction size from capillary tube model for internal stability assessment of granular soils." *Soils Found.* 56 (2): 315–320. https://doi.org/10.1016/j.sandf.2016.02.013.

Di Felice, R. 1994. "The voidage function for fluid-particle interaction systems." *Int. J. Multiphase Flow* 20 (1): 153–159. https://doi.org/10.1016/0301-9322(94)90011-6.

Douillet-Grellier, T., S. Leclaire, D. Vidal, F. Bertrand, and F. De Vuyst. 2019. "Comparison of multiphase SPH and LBM approaches for the simulation of intermittent flows." *Comput. Part. Mech.* 6 (Oct): 695–720. https://doi.org/10.1007/s40571-019-00250-3.

Elias, J. 2014. "Simulation of railway ballast using crushable polyhedral particles." *Powder Technol.* 264: 458–465. https://doi.org/10.1016/j.powtec.2014.05.052.

Eppinger, T., K. Seidler, and M. Kraume. 2011. "DEM-CFD simulations of fixed bed reactors with small tube to particle diameter ratios." *Chem. Eng. J.* 166: 324–331.

Ersoy, A., and M. Waller. 1995. "Textural characterisation of rocks." *Eng. Geol.* 39 (3–4): 123–136. https://doi.org/10.1016/0013-7952(95)00005-Z.

Feng, Z.-G., and E. E. Michaelides. 2004. "The immersed boundary-lattice Boltzmann method for solving fluid–particles interaction problems." *J. Comput. Phys.* 195 (2): 602–628. https://doi.org/10.1016/j.jcp.2003.10.013.

Fleshman, M. S., and J. D. Rice. 2014. "Laboratory modeling of the mechanisms of piping erosion initiation." *J. Geotech. Geoenviron. Eng.* 140 (6): 04014017. https://doi.org/10.1061/(ASCE)GT.1943-5606.0001106.

Guises, R., J. Xiang, J.-P. Latham, and A. Munjiza. 2009. "Granular packing: Numerical simulation and the characterisation of the effect of particle shape." *Granular Matter* 11 (Oct): 281–292. https://doi.org/10.1007/s10035-009-0148-0.

Guo, Y., Y. Yang, and X. Yu. 2018. "Influence of particle shape on the erodibility of non-cohesive soil: Insights from coupled CFD–DEM simulations." *Particuology* 39 (Aug): 12–24. https://doi.org/10.1016/j.partic.2017.11.007.

Hager, A., C. Kloss, S. Pirker, and C. Goniva. 2014. "Parallel resolved open source CFD-DEM: Method, validation and application." *J. Comput. Multiphase Flows* 6 (1): 13–27. https://doi.org/10.1260/1757-482X.6.1.13.

Hentschel, M., and N. Page. 2003. "Selection of descriptors for particle shape characterization." *Part. Part. Syst. Char.* 20 (1): 25–38. https://doi.org/10.1002/ppsc.200390002.

Hu, Z., Y. Zhang, and Z. Yang. 2019. "Suffusion-induced deformation and microstructural change of granular soils: A coupled CFD–DEM study." *Acta Geotech.* 14 (3): 795–814. https://doi.org/10.1007/s11440-019-00789-8.

Huang, X., K. J. Hanley, C. O'Sullivan, and F. C. Y. Kwok. 2014. "Effect of sample size on the response of DEM samples with a realistic grading." *Particuology* 15 (Aug): 107–115. https://doi.org/10.1016/j.partic.2013.07.006.

Indraratna, B., V. T. Nguyen, and C. Rujikiatkamjorn. 2011. "Assessing the potential of internal erosion and suffusion of granular soils." *J. Geotech. Geoenviron. Eng.* 137 (5): 550–554. https://doi.org/10.1061/(ASCE)GT.1943-5606.0000447.

Indraratna, B., A. K. Raut, and H. Khabbaz. 2007. "Constriction-based retention criterion for granular filter design." *J. Geotech. Geoenviron. Eng.* 133 (3): 266–276. https://doi.org/10.1061/(ASCE)1090-0241(2007)133:3(266).

Israr, J., B. Indraratna, and C. Rujikiatkamjorn. 2016. "Laboratory investigation of the seepage induced response of granular soils under static and cyclic loading." *Geotech. Test. J.* 39 (5): 795–812. https://doi.org/10.1520/GTJ20150288.

Jung, J., S. C. Cao, Y.-H. Shin, R. I. Al-Raoush, K. Alshibli, and J.-W. Choi. 2018. "A microfluidic pore model to study the migration of fine particles in single-phase and multi-phase flows in porous media." *Microsyst. Technol.* 24 (Feb): 1071–1080. https://doi.org/10.1007/s00542-017-3462-1.

Kang, S. K., and Y. A. Hassan. 2011. "A comparative study of direct-forcing immersed boundary-lattice Boltzmann methods for stationary complex boundaries." *Int. J. Numer. Methods Fluids* 66 (9): 1132–1158. https://doi.org/10.1002/fld.2304.

Ke, L., and A. Takahashi. 2014. "Triaxial erosion test for evaluation of mechanical consequences of internal erosion." *Geotech. Test. J.* 37 (2): 347–364. https://doi.org/10.1520/GTJ20130049.

Kenney, T. C., and D. Lau. 1985. "Internal stability of granular filters." *Can. Geotech. J.* 22 (2): 215–225. https://doi.org/10.1139/t85-029.

Kuhn, M. R., and K. Bagi. 2009. "Specimen size effect in discrete element simulations of granular assemblies." *J. Eng. Mech.* 135 (6): 485–492. https://doi.org/10.1061/(ASCE)0733-9399(2009)135:6(485).

Lai, Z., and Q. Chen. 2019. "Reconstructing granular particles from X-ray computed tomography using the TWS machine learning tool and the level set method." *Acta Geotech.* 14 (1): 1–18. https://doi.org/10.1007/s11440-018-0759-x.

Liang, Y., C. Zeng, J.-J. Wang, M.-W. Liu, T.-C. Jim Yeh, and Y.-Y. Zha. 2017. "Constant gradient erosion apparatus for appraisal of piping behavior in upward seepage flow." *Geotech. Test. J.* 40 (4): 20150282. https://doi.org/10.1520/GTJ20150282.

Link, J. M., L. A. Cuypers, N. G. Deen, and J. A. M. Kuipers. 2005. "Flow regimes in a spout–fluid bed: A combined experimental and simulation study." *Chem. Eng. Sci.* 60 (13): 3425–3442. https://doi.org/10.1016/j.ces.2005.01.027.

Liu, X., J. Gan, W. Zhong, and A. Yu. 2020a. "Particle shape effects on dynamic behaviors in a spouted bed: CFD-DEM study." *Powder Technol.* 361 (Feb): 349–362. https://doi.org/10.1016/j.powtec.2019.07.099.

Liu, Y., L. Wang, Y. Hong, J. Zhao, and Z.-Y. Yin. 2020b. "A coupled CFD-DEM investigation of suffusion of gap graded soil: Coupling effect of confining pressure and fines content." *Int. J. Numer. Anal. Methods Geomech.* 44 (18): 2473–2500. https://doi.org/10.1002/nag.3151.

Liu, Y., Z.-Y. Yin, L. Wang, and Y. Hong. 2021. "A coupled CFD–DEM investigation of internal erosion considering suspension flow." *Can. Geotech. J.* 58 (9): 1411–1425. https://doi.org/10.1139/cgj-2020-0099.

Liu, Y., Z.-Y. Yin, and J. Yang. 2023. "Micromechanical analysis of suffusion in gap-graded granular soils considering soil heterogeneity and non-uniform seepage flow." *Comput. Geotech.* 159 (Jul): 105467. https://doi.org/10.1016/j.compgeo.2023.105467.

Ma, H., L. Xu, and Y. Zhao. 2017. "CFD-DEM simulation of fluidization of rod-like particles in a fluidized bed." *Powder Technol.* 314 (Jun): 355–366. https://doi.org/10.1016/j.powtec.2016.12.008.

Maroof, M. A., A. Mahboubi, and A. Noorzad. 2021. "Effects of grain morphology on suffusion susceptibility of cohesionless soils." *Granular Matter* 23 (Feb): 1–20. https://doi.org/10.1007/s10035-020-01075-1.

Marot, D., F. Bendahmane, and H. H. Nguyen. 2012. "Influence of angularity of coarse fraction grains on internal erosion process." *La Houille Blanche* 6 (1): 47–53. https://doi.org/10.1051/lhb/2012040.

Moffat, R., R. J. Fannin, and S. J. Garner. 2011. "Spatial and temporal progression of internal erosion in cohesionless soil." *Can. Geotech. J.* 48 (3): 399–412. https://doi.org/10.1139/T10-071.

Nguyen, C. D., N. Benahmed, E. Andò, L. Sibille, and P. Philippe. 2019. "Experimental investigation of microstructural changes in soils eroded by suffusion using X-ray tomography." *Acta Geotech.* 14 (Jun): 749–765. https://doi.org/10.1007/s11440-019-00787-w.

Pal, S., and A. A. Kulkarni. 2023. "Settling and spreading behaviour of particle clusters in quiescent liquids in confined vessels." *Particuology* 83 (Dec): 91–100. https://doi.org/10.1016/j.partic.2023.01.019.

Peskin, C. S. 1972. "Flow patterns around heart valves: A numerical method." *J. Comput. Phys.* 10 (2): 252–271. https://doi.org/10.1016/0021-9991(72)90065-4.

Press, W. H., S. A. Teukolsky, W. T. Vetterling, and B. P. Flannery. 1992. *Numerical recipes in C: The art of scientific computing*. 2nd ed. Cambridge, UK: Cambridge University Press.

Qian, J.-G., C. Zhou, Z.-Y. Yin, and W.-Y. Li. 2021. "Investigating the effect of particle angularity on suffusion of gap-graded soil using coupled CFD-DEM." *Comput. Geotech.* 139 (Nov): 104383. https://doi.org/10.1016/j.compgeo.2021.104383.

Salot, C., P. Gotteland, and P. Villard. 2009. "Influence of relative density on granular materials behavior: DEM simulations of triaxial tests." *Granular Matter* 11 (4): 221–236. https://doi.org/10.1007/s10035-009-0138-2.

Shen, Z., G. Wang, D. Huang, and F. Jin. 2022. "A resolved CFD-DEM coupling model for modeling two-phase fluids interaction with irregularly shaped particles." *J. Comput. Phys.* 448 (Jan): 110695. https://doi.org/10.1016/j.jcp.2021.110695.

Shire, T., C. O'Sullivan, K. J. Hanley, and R. J. Fannin. 2014. "Fabric and effective stress distribution in internally unstable soils." *J. Geotech. Geoenviron. Eng.* 140 (12): 04014072. https://doi.org/10.1061/(ASCE)GT.1943-5606.0001184.

Sibille, L., D. Marot, and Y. Sail. 2015. "A description of internal erosion by suffusion and induced settlements on cohesionless granular matter." *Acta Geotech.* 10 (Dec): 735–748. https://doi.org/10.1007/s11440-015-0388-6.

Slangen, P., and R. J. Fannin. 2017. "The role of particle type on suffusion and suffusion." *Géotech. Lett.* 7 (Mar): 6–10. https://doi.org/10.1680/jgele.16.00099.

Suh, H. S., K. Y. Kim, J. Lee, and T. S. Yun. 2017. "Quantification of bulk form and angularity of particle with correlation of shear strength and packing density in sands." *Eng. Geol.* 220 (Mar): 256–265. https://doi.org/10.1016/j.enggeo.2017.02.015.

Tao, J., and H. Tao. 2017. "Factors affecting piping erosion resistance: Revisited with a numerical modeling approach." *Int. J. Geomech.* 17 (11): 04017097. https://doi.org/10.1061/(ASCE)GM.1943-5622.0000999.

Valdes, J. R., and J. C. Santamarina. 2006. "Particle clogging in radial flow: Microscale mechanisms." *SPE J.* 11 (2): 193–198. https://doi.org/10.2118/88819-PA.

Wang, T., F. Zhang, J. Furtney, and B. Damjanac. 2022. "A review of methods, applications and limitations for incorporating fluid flow in the discrete element method." *J. Rock Mech. Geotech. Eng.* 14 (3): 1005–1024. https://doi.org/10.1016/j.jrmge.2021.10.015.

Wautier, A., S. Bonelli, and F. Nicot. 2019. "DEM investigations of internal erosion: Grain transport in the light of micromechanics." *Int. J. Numer. Anal. Methods Geomech.* 43 (1): 339–352. https://doi.org/10.1002/nag.2866.

Wei, D., J. Wang, and B. Zhao. 2018. "A simple method for particle shape generation with spherical harmonics." *Powder Technol.* 330 (May): 284–291. https://doi.org/10.1016/j.powtec.2018.02.006.

Xiao, T., N. Qin, Z. Lu, X. Sun, M. Tong, and Z. Wang. 2017. "Development of a smoothed particle hydrodynamics method and its application

to aircraft ditching simulations." *Aerosp. Sci. Technol.* 66 (Jul): 28–43. https://doi.org/10.1016/j.ast.2017.02.022.

Xiong, H., H. Wu, X. Bao, and J. Fei. 2021. "Investigating effect of particle shape on suffusion by CFD-DEM modeling." *Constr. Build. Mater.* 289 (Jun): 123043. https://doi.org/10.1016/j.conbuildmat.2021.123043.

Yin, Z.-Y., P. Wang, and F. Zhang. 2020. "Effect of particle shape on the progressive failure of shield tunnel face in granular soils by coupled FDM-DEM method." *Tunnelling Underground Space Technol.* 100 (Jun): 103394. https://doi.org/10.1016/j.tust.2020.103394.

Zhao, B. D., D. H. Wei, and J. F. Wang. 2017. "Particle shape quantification using rotation-invariant spherical harmonic analysis." *Géotech. Lett.* 7 (2): 190–196. https://doi.org/10.1680/jgele.17.00011.

Zhao, S., X. Zhou, and W. Liu. 2015. "Discrete element simulations of direct shear tests with particle angularity effect." *Granular Matter* 17 (Dec): 793–806. https://doi.org/10.1007/s10035-015-0593-x.

Zhou, B., and J. Wang. 2017. "Generation of a realistic 3D sand assembly using X-ray micro-computed tomography and spherical harmonic-based principal component analysis." *Int. J. Numer. Anal. Methods Geomech.* 41 (1): 93–109. https://doi.org/10.1002/nag.2548.

Zhou, C., J.-G. Qian, Z.-Y. Yin, Y.-J. Liu, and Z.-B. Du. 2023. "Effect of particle shape and bedding angle on suffusion in gap-graded granular soils by coupled CFD-DEM method." *Int. J. Numer. Anal. Methods Geomech.* 47 (8): 1373–1398. https://doi.org/10.1002/nag.3519.